

# $^{19}\text{F}$ Electron-Nuclear Double Resonance Reveals Interaction between Redox-Active Tyrosines across the $\alpha/\beta$ Interface of *E. coli* Ribonucleotide Reductase

Andreas Meyer,\* Annemarie Kehl, Chang Cui, Fehmke A. K. Reichardt, Fabian Hecker, Lisa-Marie Funk, Manas K. Ghosh, Kuan-Ting Pan, Henning Urlaub, Kai Tittmann, JoAnne Stubbe,\* and Marina Bennati\*



Cite This: *J. Am. Chem. Soc.* 2022, 144, 11270–11282



Read Online

ACCESS |



Metrics & More

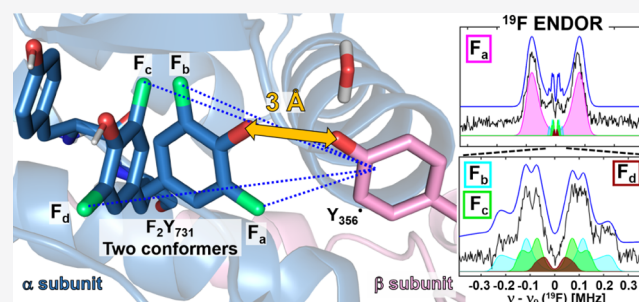


Article Recommendations



Supporting Information

**ABSTRACT:** Ribonucleotide reductases (RNRs) catalyze the reduction of ribonucleotides to deoxyribonucleotides, thereby playing a key role in DNA replication and repair. *Escherichia coli* class Ia RNR is an  $\alpha_2\beta_2$  enzyme complex that uses a reversible multistep radical transfer (RT) over 32 Å across its two subunits,  $\alpha$  and  $\beta$ , to initiate, using its metallo-cofactor in  $\beta_2$ , nucleotide reduction in  $\alpha_2$ . Each step is proposed to involve a distinct proton-coupled electron-transfer (PCET) process. An unresolved step is the RT involving  $\text{Y}_{356}(\beta)$  and  $\text{Y}_{731}(\alpha)$  across the  $\alpha/\beta$  interface. Using 2,3,5- $\text{F}_3\text{Y}_{122}\text{-}\beta_2$  with 3,5- $\text{F}_2\text{Y}_{731}\text{-}\alpha_2$ , GDP (substrate) and TTP (allosteric effector), a  $\text{Y}_{356}^\bullet$  intermediate was trapped and its identity was verified by 263 GHz electron paramagnetic resonance (EPR) and 34 GHz pulse electron–electron double resonance spectroscopies. 94 GHz  $^{19}\text{F}$  electron-nuclear double resonance spectroscopy allowed measuring the interspin distances between  $\text{Y}_{356}^\bullet$  and the  $^{19}\text{F}$  nuclei of 3,5- $\text{F}_2\text{Y}_{731}$  in this RNR mutant. Similar experiments with the double mutant  $\text{E}_{52}\text{Q}/\text{F}_3\text{Y}_{122}\text{-}\beta_2$  were carried out for comparison to the recently published cryo-EM structure of a holo RNR complex. For both mutant combinations, the distance measurements reveal two conformations of 3,5- $\text{F}_2\text{Y}_{731}$ . Remarkably, one conformation is consistent with 3,5- $\text{F}_2\text{Y}_{731}$  within the H-bond distance to  $\text{Y}_{356}^\bullet$ , whereas the second one is consistent with the conformation observed in the cryo-EM structure. The observations unexpectedly suggest the possibility of a colinear PCET, in which electron and proton are transferred from the same donor to the same acceptor between  $\text{Y}_{356}$  and  $\text{Y}_{731}$ . The results highlight the important role of state-of-the-art EPR spectroscopy to decipher this mechanism.



## 1. INTRODUCTION

Ribonucleotide reductases (RNRs) catalyze the conversion of four nucleoside di- or triphosphates (ND(T)Ps) to deoxyribonucleoside di- or triphosphates (dND(T)Ps) in all organisms (Figure 1).<sup>1–3</sup> RNRs are highly regulated enzymes playing an important role in controlling the ratio and relative amounts of dNTPs essential for the fidelity of DNA replication and repair. Imbalance in dNTP pools results in genomic instability and leads to disease states.<sup>4–6</sup> RNRs' essential role has made them targets for cancer and, more recently, antibiotic therapeutics.<sup>6–12</sup>

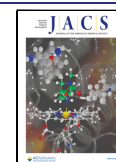
The *E. coli* class Ia RNR, a prototype model system for human RNR,<sup>6</sup> is composed of two subunits,  $\alpha$ <sup>13</sup> and  $\beta$ ,<sup>14</sup> both required for activity. Based on their  $\alpha_2$  and  $\beta_2$  structures, Uhlin and Eklund proposed a symmetrical  $\alpha_2\beta_2$  docking model (Figure 2A) for active RNR, which has played a central role in the experimental design.<sup>13</sup> The model for substrate activation and chemistry requires that the diferric tyrosyl radical ( $\text{Y}_{122}^\bullet$ ) cofactor located in  $\beta_2$  oxidizes  $\text{C}_{439}$  to a thiyl radical in the

active site of  $\alpha_2$ , which, in turn, initiates NDP reduction (Figures 1 and 2C). Thiyl radical formation is proposed to occur by a radical transfer (RT) pathway, which involves five or six radical intermediates (Figure 2C),<sup>15</sup> each generated by proton-coupled electron-transfer (PCET) steps.<sup>16–19</sup>

Central for developing this model has been the ability to replace pathway Ys site-selectively with unnatural amino acids (UAAs) that have allowed the generation and thermodynamic trapping of pathway radical intermediates. The tyrosyl radicals ( $\text{Y}^\bullet$ s) were studied by a suite of multifrequency electron paramagnetic resonance (EPR)<sup>20–30</sup> methods as well as by

Received: March 17, 2022

Published: June 2, 2022



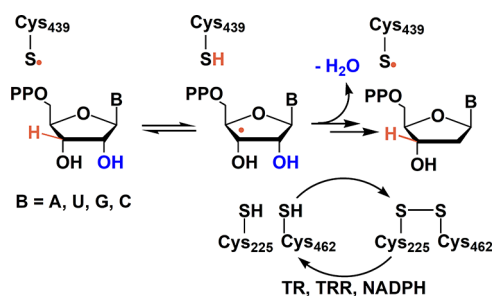


**Figure 1.** Reduction of NDPs to dNDPs catalyzed by *Escherichia coli* class Ia RNR. The reduction is initiated by a thiyl radical ( $C_{439}^{\bullet}$ ), and the reducing equivalents are provided by the oxidation of  $C_{225}$  and  $C_{462}$  to a disulfide. Multiple turnovers require a redox reducing system such as thioredoxin (TR), thioredoxin reductase (TRR), and nicotinamide adenine dinucleotide phosphate (NADPH).

transient absorption spectroscopic methods using photo- $\beta_2$  RNRs.<sup>30–34</sup>

Despite much insight into nature's design for radical initiation in RNRs, elucidating the molecular basis for the RT across the  $\alpha/\beta$  subunit interface has been hampered by the lack of structural information about the C-terminal tail of all  $\beta$ s (residues 341–375 in *E. coli* RNR), essential for  $\alpha/\beta$  subunit interaction.<sup>35–37</sup> The location of  $Y_{356}$  in the RT pathway within this tail was thus unknown. Recently, a near-atomic resolution cryo-EM structure of a trapped  $\alpha_2\beta_2$  *E. coli* complex was obtained (Figure 2B).<sup>38</sup> It was generated from the incubation of a double mutant of  $\beta_2$ ,  $E_{52}Q/F_3Y_{122}\beta_2$ , with *wt*- $\alpha_2$  substrate (GDP), and allosteric effector (TTP) with freeze-quenching at 50 s. The 2,3,5- $F_3Y_{122}$  substitution allowed the generation of one dGDP product and accumulation of one pathway radical at  $Y_{356}^{\bullet}$ . The  $E_{52}Q$  mutation was important for successfully trapping the  $\alpha_2\beta_2$  complex. The  $E_{52}$  residue resides

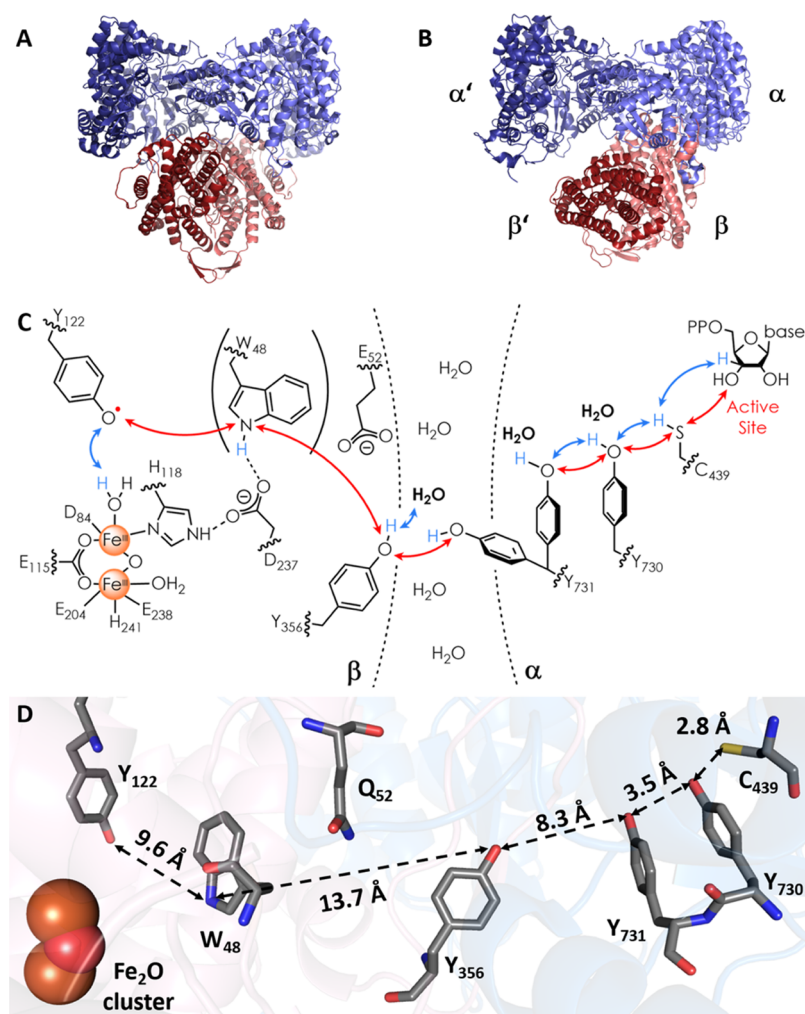


**Figure 2.** Docking model<sup>13</sup> (A) and cryo-EM structure<sup>38</sup> (B) of the  $\alpha_2\beta_2$  complex of *E. coli* class Ia RNR and the proposed RT pathway, (C) and (D), respectively. (A) The docking model based on the shape complementarity of subunits  $\alpha_2$ <sup>13</sup> and  $\beta_2$ .<sup>14</sup> (B) Cryo-EM structure of an  $\alpha_2\beta_2$  complex of RNR generated when  $E_{52}Q/F_3Y_{122}\beta_2$ , *wt*- $\alpha_2$  GDP (substrate) and TTP (effector) were quenched at 50 s (pdb code: 6W4X).<sup>38</sup> Asymmetry of the complex is indicated by  $\alpha'\beta'$  (disordered pair) and  $\alpha\beta$  (ordered pair). (C) The proposed forward RT pathway based on many experiments.<sup>20–27,30–33</sup>  $W_{48}$  is shown in parentheses as there currently is no direct evidence for its involvement. The red and blue double arrows describe electron and proton transfers, respectively. Evidence for the bold water molecules has been reported recently.<sup>27,28</sup> (D) An intact RT pathway within  $\alpha\beta$  including  $Y_{356}$  and its position relative to  $Y_{731}$  is visible for the first time in the cryo-EM structure.<sup>38</sup> Distances between RT residues are indicated; the  $^{19}F$  atoms of 2,3,5- $F_3Y_{122}$  present in the cryo-EM structure have been omitted. Interfacial residue  $Q_{52}$  ( $E_{52}$  in *wt*-RNR) is included as it was important for stabilizing the  $\alpha_2\beta_2$  complex in the cryo-EM experiment.

at the  $\alpha/\beta$ -interface and is essential for activity, enabling proton release during  $Y_{356}$  oxidation in the RT.<sup>33,39</sup>

The cryo-EM structure (Figure 2B) revealed an asymmetric  $\alpha_2\beta_2$  complex, consistent with earlier results.<sup>37,40</sup> It also revealed the residues in the C-terminal tail of  $\beta$  (341–375) in an ordered  $\alpha\beta$  pair, the intact RT pathway including the location of  $Y_{356}$  and its location relative to  $Y_{731}(\alpha)$  (Figure 2D) for the first time. The entire C-terminal tail in  $\alpha'/\beta'$ , where chemistry has occurred and  $Y_{356}^\bullet$  is supposedly trapped, remains disordered.

The importance of  $Y_{356}$  during RT has been established by many different methods that often led to the detection of the  $Y_{356}^\bullet$  intermediate. Recent studies to identify the proton acceptor during its oxidation in forward RT revealed that the most reasonable candidates,  $E_{52}(\beta)$  and  $E_{350}(\beta)$ , both conserved and essential,<sup>36,39,41</sup> are unlikely to be the ultimate acceptors.<sup>33,34,42</sup> These residues are located at  $\sim 7$  Å ( $E_{52}$ ) and  $\sim 14$  Å ( $E_{350}$ ) distances from the phenol-oxygen atom of  $Y_{356}$  in the ordered  $\alpha\beta$  pair of the cryo-EM structure,<sup>38</sup> too far for direct proton or H atom transfer with  $Y_{356}^\bullet$ .<sup>43</sup> A variety of  $^1\text{H}$  and  $^{17}\text{O}$  high-frequency electron-nuclear double resonance (ENDOR) experiments on  $Y_{356}^\bullet$ ,<sup>27,28</sup> kinetic studies using RNRs with  $F_nY_{356}$ <sup>33</sup> and a photo-oxidant appended to the  $C_{355}$  mutant of  $\beta$ , and pH studies of  $Y_{356}^\bullet$  formation using  $F_2Y_{356}$ <sup>42</sup> all support the interaction of  $Y_{356}^\bullet$  with water (Figure 2C).

Efforts to understand the residues involved in managing the proton to support the PCET between  $Y_{356}$  and  $Y_{731}$  across the  $\alpha/\beta$  interface have been less successful. The cryo-EM structure shows an O–O distance between  $Y_{356}$  and  $Y_{731}$  of  $\sim 8$  Å in ordered  $\alpha\beta$ , with  $Y_{731}$  in its unusual stacked conformation with  $Y_{730}$  as in previous X-ray structures of  $\alpha_2$  alone.<sup>13</sup> While a number of pulsed electron double resonance (PELDOR) experiments<sup>6</sup> revealed sharp distance distributions consistent with little  $Y_{356}^\bullet$  flexibility, several different experiments reported the mobility of  $Y_{731}$ . In a crystal structure of  $\text{NH}_2Y_{730}\text{-}\alpha_2$  alone,  $Y_{731}$  was found in a conformation where it is flipped away from the stacked conformation with  $\text{NH}_2Y_{730}$ .<sup>44</sup> PELDOR studies on a double mutant  $R_{411}A\text{-NH}_2Y_{731}\text{-}\alpha_2$  under turnover conditions revealed a conformational change of 3 Å in trapped  $\text{NH}_2Y_{731}^\bullet$ , consistent with a flipping toward the  $\alpha/\beta$  interface.<sup>26</sup> Subsequent studies using photo- $\beta_2$  with the same  $\alpha_2$  mutations revealed dynamic/rapid conformational changes of  $Y_{731}$ .<sup>30</sup> Another EPR study by Yokoyama et al. suggested the flipping of  $F_2Y_{731}^\bullet$ ,<sup>23</sup> which was trapped as a minority radical species in  $\text{NO}_2Y_{122}\text{-}\beta_2/F_2Y_{731}\text{-}\alpha_2$ . Molecular dynamics (MD) simulations using the cryo-EM structure and the  $\alpha/\beta$  interface in water also support the flexibility of  $Y_{731}$ ,<sup>45</sup> with movement away from the stacked conformation with  $Y_{730}$ . The studies together support a model for PCET between  $Y_{356}^\bullet$  and  $Y_{731}$  across the  $\alpha/\beta$  interface that could involve a movement of  $Y_{731}$  toward the interface (Figure 2C), with consequences for their PCET chemistry. However, structural or spectroscopic evidence for interaction between  $Y_{356}^\bullet$  and  $Y_{731}$  has never been observed.

In this article, we use  $^{19}\text{F}\text{-Y}$  analogues introduced site-specifically into *E. coli* RNR,  $F_3Y_{122}\text{-}\beta_2$  (or the double mutant  $E_{52}Q/F_3Y_{122}\text{-}\beta_2$ ), incubated with 3,5- $F_2Y_{731}\text{-}\alpha_2$ , GDP, and TTP to generate and trap  $Y_{356}^\bullet$ .  $F_2Y_{731}$  was chosen for its symmetric  $^{19}\text{F}$  substitution pattern and minimally perturbed reduction potential relative to  $Y$ .<sup>46,47</sup> The  $Y_{356}^\bullet$  location and identity are established using 34 GHz PELDOR and 263 GHz EPR spectroscopies, respectively.  $^{19}\text{F}$  ENDOR spectroscopy<sup>48,49</sup> at 94 GHz is used in an effort to determine the distances across

the subunit interface between the trapped  $Y_{356}^\bullet(\beta)$  and the  $^{19}\text{F}$  nuclei of  $F_2Y_{731}(\alpha)$ . The ENDOR spectra give unambiguous evidence for two conformations of  $F_2Y_{731}$ . One conformation is consistent with the structure observed by cryo-EM (ordered  $\alpha\beta$  pair). The second conformation indicates a flipping of  $F_2Y_{731}$  toward  $Y_{356}^\bullet$ . The results have important implications for the PCET mechanism across the  $\alpha/\beta$  interface.

## 2. MATERIALS AND METHODS

**2.1. Preparation of RNR Mutants and Activity Assays.** The RNR mutants  $F_3Y_{122}\text{-}\beta_2$ ,  $E_{52}Q/F_3Y_{122}\text{-}\beta_2$ ,  $F_2Y_{731}\text{-}\alpha_2$ , and  $^{17}\text{O}\text{-Y}\text{-wt-}\alpha_2$  were expressed and purified, as previously described.<sup>39,44,50</sup> Activities of  $(E_{52}Q)F_3Y_{122}\text{-}\beta_2/F_2Y_{731}\text{-}\alpha_2$  and  $\text{wt-}\beta_2/^{17}\text{O}\text{-Y}\text{-}\alpha_2$  were determined using the spectrophotometric assay (Supporting Information (SI) 1, Table S1).<sup>51</sup>

**2.2. EPR Sample Preparation.** The  $Y_{356}^\bullet$  intermediate was trapped by incubating a solution of  $F_2Y_{731}\text{-}\alpha_2$ , GDP, and TTP in assay buffer (50 mM HEPES, 15 mM  $\text{MgSO}_4$ , 1 mM EDTA, pH 7.6) with  $F_3Y_{122}\text{-}\beta_2$  or  $E_{52}Q/F_3Y_{122}\text{-}\beta_2$  in assay buffer. Glycerol concentrations were optimized (Figure S1) and typically added to  $\sim 20\%$  of the final volume to prolong phase memory times  $T_M$  for PELDOR and ENDOR measurements. The final concentrations were  $\sim 80$   $\mu\text{M}$   $\alpha_2\beta_2$ ,  $\sim 1$  mM GDP, and  $\sim 200$   $\mu\text{M}$  TTP. The reaction mixture was transferred to either 34 GHz EPR tubes (Q-band) (12  $\mu\text{L}$ , 1.5 mm inner diameter (ID) Suprasil tube, Wilmad) or 94 GHz (W-band) tubes (4.4  $\mu\text{L}$ , 0.7 mm ID clear fused quartz tubes) and quenched by freezing in liquid nitrogen at reaction times ( $T_Q$ ) of 40–80 s (Q-band) or 35–55 s (W-band). A second set of samples were prepared with  $T_Q > 100$  s. Two hundred and sixty-three GHz EPR samples were prepared in Suprasil capillaries (ID 0.2 mm, Vitrocom) without glycerol and quenched at  $T_Q = 15\text{--}20$  s. All samples are summarized in SI 2, Table S2.

**2.3. 263 GHz EPR Spectroscopy.** High-frequency (HF) 263 GHz echo-detected EPR spectra were recorded with a commercial spectrometer, as previously reported.<sup>52</sup> Details on the spectral acquisition are given in SI 3.

**2.4. 34 GHz PELDOR Spectroscopy.** Four-pulse PELDOR experiments<sup>53,54</sup> were performed at 34 GHz (Q-band) on a commercial Bruker ELEXSYS E580 EPR spectrometer, as previously reported.<sup>27</sup> An optimized temperature of 50 K was selected, where high sensitivity is achieved and unreacted  $F_3Y_{122}^\bullet$  does not contribute to the spin echo under conditions used for data collection (SI 4.1–4.3). MW pulses were amplified by a pulsed 170 W TWT amplifier (Model 187Ka, Applied Systems Engineering) with typical pulse lengths of 14–16 ns for the pump  $\pi$ -pulse at the center of the overcoupled resonator. The observer frequency was set to  $-105$  MHz from the dip center, leading to observer  $\pi$ -pulse lengths of 24–28 ns. The  $\tau_1$  value was 250 ns, and  $\tau_2$  values were optimized based on  $T_M$  measurements (SI 4.2). Shot repetition times were 4–6 ms. Time traces were recorded at three different observer positions (Figure S5) and their intensities were summed, reflecting their respective EPR signal strengths at that excitation position. Traces were analyzed with DeerAnalysis 2019,<sup>55</sup> using Tikhonov regularization ( $L$ -curve criterion for  $\alpha$  parameter) and checked for consistency using neural network analysis.<sup>56,57</sup>

**2.5. 94 GHz ENDOR Spectroscopy.** Pulsed EPR and ENDOR experiments at 94 GHz (W-band) were performed on a commercial Bruker ELEXSYS E680 EPR spectrometer, as previously described.<sup>23</sup> Using a 2 W MW amplifier, typical  $\pi/2$  pulse lengths of 10–12 ns were achieved. EPR (echo-detected) spectra and signal contributions are illustrated in SI 5.1. Shot repetition times were optimized to 2–4 ms based on  $T_1$  measurements (SI 5.2).

$^{19}\text{F}$  Mims ENDOR spectra of the  $Y_{356}^\bullet$  were recorded using radio frequency (RF) pulses amplified by a 250 W RF amplifier (250A250A Amplifier Research). RF pulse lengths of 22  $\mu\text{s}$  were used for  $^{19}\text{F}$  nuclei with  $\sim 1.6$  MHz couplings or 44  $\mu\text{s}$  for couplings  $\leq 250$  kHz. RF pulse lengths were optimized using Rabi nutation experiments. Stochastic RF acquisition<sup>58–60</sup> with 20 shots per point was used. To observe  $^{19}\text{F}$  couplings of different sizes, the adjustment of the

interpulse delay  $\tau$  in the Mims sequence was crucial. For couplings on the order of 1.6 MHz, two measurements with  $\tau$  values of 236 and 266 ns were performed and summed subsequently (normalized to the number of scans) to attenuate the proton background. For smaller couplings,  $\leq \sim 250$  kHz,  $\tau$  was optimized to 620–622 ns (SI 5.3). ENDOR spectra were recorded at three different observer positions (Figure S8) and summed up with intensities reflecting their respective EPR signal strengths at that excitation position.

Data were collected at two temperatures. At 50 K, ENDOR sensitivity was higher than that at 80 K, where usually the signal of unreacted  $F_3Y_{122}^\bullet$  disappears due to faster relaxation.<sup>27</sup> As a downside, at 50 K, the unreacted  $F_3Y_{122}^\bullet$  contributed to the echo intensity of the Mims sequence at short interpulse delays  $\tau$ . The contribution of  $F_3Y_{122}^\bullet$  led to  $^{19}F$  ENDOR background signals, which had to be removed during data processing (SI 5.4). As a control for the background correction procedure, we repeated representative  $^{19}F$  ENDOR measurements at 80 K (SI 5.5–5.6) where no background of  $F_3Y_{122}^\bullet$  was present. The results obtained at 50 and 80 K are fully consistent. In addition to the  $^{19}F$  background, broad, overlapping  $^1H$  resonances associated with the 3,5-H atoms of  $Y_{356}^\bullet$  were identified by their changes observed with  $\tau$  value changes and they were subtracted from the  $^{19}F$  spectra, as illustrated in SI 5.4.

$^{17}O$  ENDOR control experiments were performed using similar parameters described in our recent  $^{17}O$  ENDOR study<sup>28</sup> and are reported in SI 6.

**2.6. Simulations of ENDOR Data.** Mims ENDOR simulations of the  $Y_{356}^\bullet$  were performed using EasySpin's saffron routine.<sup>61</sup> The  $g$  tensor was  $g_x = 2.0062$ ,  $g_y = 2.0044$ , and  $g_z = 2.0022$ .<sup>27</sup> In the molecular frame,  $g_x$  is aligned along the C–O $\bullet$  bond of  $Y_{356}^\bullet$ , while  $g_y$  is perpendicular to this direction and in the plane of the aromatic ring. The strongly coupled  $\beta$ -proton of  $Y_{356}^\bullet$  was included using previously reported hyperfine coupling (HFC) parameters.<sup>27</sup> For simulating the  $^{19}F$  ENDOR spectra with  $\tau = 620$ – $622$  ns, the C3 and C5 protons<sup>27</sup> of  $Y_{356}^\bullet$  were included. The  $^{19}F$  ENDOR line width parameter was simulated as 25 kHz for couplings below 0.5 MHz.<sup>49</sup> For larger couplings, a line width of 250 kHz was used. Chemical shift anisotropies were not resolved in the 94 GHz  $^{19}F$  ENDOR spectra.<sup>62</sup>

**2.7. Structural Models for ENDOR Analysis.** Due to the large parameter space associated with the two Fs of  $F_2Y_{731}$  and, as will become clear, their multiple side-chain conformations, a fitting routine that generates the most likely set of HFC parameters by minimizing residuals (rmsd) is not possible. We therefore used an approach similar to that described previously to analyze the PCET steps within  $\alpha_2$  using  $NH_2Y_{731}$  and the X-ray structure of  $\alpha_2$  to position  $Y_{730}$  and  $C_{439}$ .<sup>25</sup> In the present case, the small models were constructed starting from pdb 6W4X, the recent cryo-EM structure (resolution 3.3–5.5 Å).<sup>38</sup>  $Y_{356}$  from  $\beta$  and  $Y_{731}$  and  $Y_{730}$  from  $\alpha$  were extracted from the ordered  $\alpha/\beta$  pair (Figure 2B,D).  $^{19}F$  atoms at C3 and C5 of  $Y_{731}$  were introduced using PyMOL.<sup>63</sup> The peptide bonds connecting each tyrosine to their protein backbone were replaced by NHR and –CRO (Figure 3) groups, and their  $xyz$  coordinates were not changed compared to the cryo-EM structure. Density functional theory (DFT)-based, constrained geometry optimization using ORCA<sup>64</sup> resulted in the model structure S1 of the triad  $Y_{356}$ – $F_2Y_{731}$ – $Y_{730}$ . Further representative conformations of the triad were obtained by rotating around  $Ca/C\beta$  and  $C\beta$ -phenol bonds displacing the phenol side chains of  $Y_{356}$  and  $F_2Y_{731}$ , as illustrated in Figure 3. Resulting models to fit the spectroscopic data are designated SX ( $X = 1, 2, 3, \dots, 5$ ) and are summarized in Tables S6 and S7 in SI 8. A water molecule binding to  $Y_{356}^\bullet$  was also introduced into each model, with a binding geometry based on our previous studies (H-bond length ca. 1.8 Å, angle C4–O $\bullet$ –H ca. 120°, C3–C4–O $\bullet$ –H dihedral ca. 20°).<sup>27,28</sup> The effect of H-bonds on the spin density distribution,<sup>65,66</sup> further technical details on the DFT calculations, and the adaptation of the DFT-predicted parameters to the ENDOR simulations are described in the results section and summarized in SI 7. Contributions of the different conformations were assessed by rmsd analysis. Orientation-selective  $^{19}F$  spectra were then simulated using one set of parameters for all spectra.

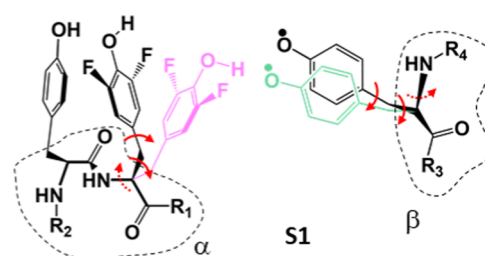


**Figure 3.** Models for the Y-triad. The black conformation corresponds to S1 but without the water molecule. The pink orientation of  $F_2Y_{731}$  illustrates a flipped conformation, and the green orientation of  $Y_{356}^\bullet$  represents a repositioning of the radical toward  $F_2Y_{731}$ , used in models S2–S5. Atom positions of the backbone are from the cryo-EM structure within  $\leq 0.5$  Å.  $R_1$ – $R_4$  peptide chains have been replaced by H atoms in S1–S5. Red arrows indicate a rotation around a bond, and dashed arrows indicate small rotations (Table S6).

### 3. RESULTS

#### 3.1. Characterization of RNR Constructs Using Activity Measurements, High-Field EPR, and PELDOR.

The first part of the investigation required examination of the new RNR constructs that contain the  $^{19}F$  labels in  $F_2Y_{731}$ . Steady-state activities are reported in Table S1. Spectrophotometric assays revealed a specific activity of 560 nmol/(mg·min) (ca. 7% of wt) for  $F_3Y_{122}$ - $\beta_2$ / $F_2Y_{731}$ - $\alpha_2$ , defined with respect to the mass of  $\beta_2$  in the assay. In contrast, an activity of only 6 nmol/(mg·min), that is, the lower limit of detection, was measured for  $E_{52}Q$ / $F_3Y_{122}$ - $\beta_2$ / $F_2Y_{731}$ - $\alpha_2$ . The latter finding was expected, as the  $E_{52}Q$  mutation disrupts steady-state activity.<sup>39</sup>

Nevertheless, both constructs are capable of one turnover and allowed trapping of the intermediate  $Y_{356}^\bullet$  for EPR samples during back-radical transfer.<sup>67</sup> Moreover, glycerol is required in the sample preparation to prolong spin relaxation in the EPR experiments. Thus, the glycerol content (v%) was also optimized based on its effect on RNR activity (SI 1) and a value of 20 v% was selected for almost all samples (SI 2, Table S2). We characterized the structure of the trapped radical in  $F_3Y_{122}$ - $\beta_2$ / $F_2Y_{731}$ - $\alpha_2$  and  $E_{52}Q$ / $F_3Y_{122}$ - $\beta_2$ / $F_2Y_{731}$ - $\alpha_2$  by 263 GHz EPR (SI 3). In all quenched reaction mixtures, two radical species were observed (Figure S2). One contribution arose from the unreacted  $F_3Y_{122}^\bullet$  and was readily identified by its large  $g_x$  value (2.0082) and its characteristic  $^{19}F$  HFC structure. After subtracting a reference spectrum of  $F_3Y_{122}^\bullet$ , the spectrum of the intermediate became visible (Figure S3). This radical was identified as  $Y_{356}^\bullet$  due to the characteristic low  $g_x$  value of 2.0062 (reference spectrum of  $Y_{356}^\bullet$  is shown in Figures S2 and S3), as reported with  $F_3Y_{122}$ - $\beta_2$ /wt- $\alpha_2$ .<sup>27</sup> The analysis of the HF-EPR spectra also revealed no other radical species.

PELDOR spectroscopy (34 GHz) was then used to measure the diagonal distance between  $Y_{356}^\bullet$  in one  $\alpha\beta$  pair and  $F_3Y_{122}^\bullet$  in the second one (Figure 4). The orientation-averaged time traces exhibit clear oscillations. Indistinguishable results were obtained for various sample preparation conditions (SI 4). For comparison, a time trace of  $F_3Y_{122}$ - $\beta_2$ /wt- $\alpha_2$  was also measured (Figure 4, green). Distance distributions with a single peak centered at  $3.03 \pm 0.02$  nm (Figure 4) and a width (full width at half-maximum (FWHM); Table S4) of 0.09–0.14 nm were obtained for all samples. The observed distance is typical for  $F_3Y_{122}^\bullet$ – $Y_{356}^\bullet$  pairs.<sup>6,27</sup> From PELDOR and HF-EPR, we

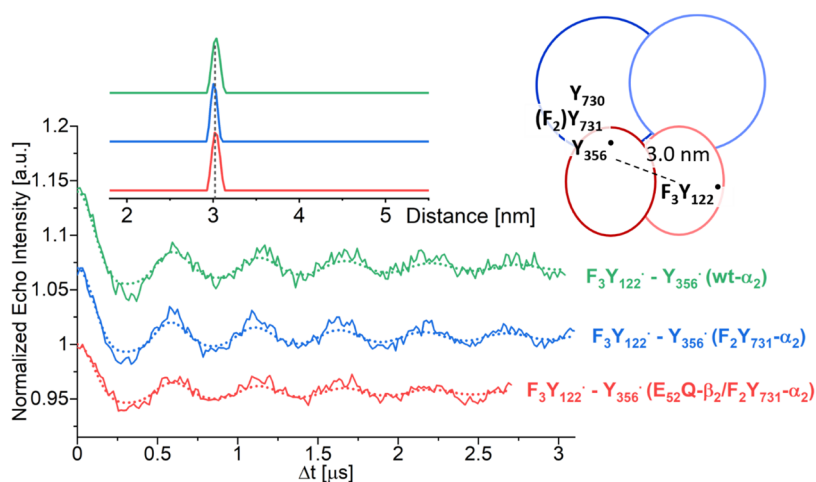


**Figure 4.** Orientation-averaged 34 GHz PELDOR time traces of  $F_3Y_{122}\beta_2/F_2Y_{731}\alpha_2$  ( $\sim 80 \mu\text{M}$ ,  $T_Q = 77 \text{ s}$ , blue line),  $E_{52}Q/F_3Y_{122}\beta_2/F_2Y_{731}\alpha_2$  ( $\sim 80 \mu\text{M}$ ,  $T_Q = 44 \text{ s}$ , red), and  $F_3Y_{122}\beta_2/wt\alpha_2$  (green) along with fits (dotted lines). Distance distributions are shown as the inset. A cartoon illustrates the assignment of distance peaks to radical pairs. A symmetric representation was chosen as the experiments reported herein do not inform about the asymmetry in the protein complex.

conclude that  $Y_{356}\bullet$  is the observed radical, as previously characterized using  $wt\alpha_2$  for incubation.<sup>27</sup>

It is interesting to consider the observed distance within the framework of the new cryo-EM structure.<sup>38</sup> The detected radical intermediate ( $Y_{356}\bullet$ ) is thought to be produced during reverse RT in the first turnover.<sup>67</sup> If the first turnover was occurring for instance in the  $\alpha'\beta'$  pair, see the notation from the cryo-EM structure (Figure 2B), then the observed PELDOR distance should be between  $Y_{356}\bullet(\beta')$  and  $F_3Y_{122}\bullet(\beta)$ . However, in the cryo-EM structure, the C-terminal  $\beta'$  tail is disordered at the interface, indicating that the trapped state might be different under the conditions of the EPR experiments. Because of the disorder, the distance between  $F_3Y_{122}\bullet(\beta)$  and  $Y_{356}\bullet(\beta')$  cannot be measured in the cryo-EM structure. If we consider the opposite diagonal distance, i.e., between the centroids<sup>68</sup> of the Tyr-O, C1, C3, and C5 atoms of  $F_3Y_{122}\bullet$  in  $\beta'$  and  $Y_{356}\bullet$  in  $\beta$ , then the PELDOR distance of 3.0 nm is in agreement with this structure. We note that many such distances have been measured with other constructs.<sup>6</sup> All give a sharp 3 nm distance feature, suggesting that the  $Y_{356}\bullet$  conformation is constrained. Our model for half-site RNR reactivity<sup>15</sup> requires that the complex interconverts to allow for alternating PCET in  $\alpha\beta$  and  $\alpha'\beta'$ . When the  $Y_{356}\bullet$  is trapped, the interconversion is slow. The kinetics of this structural interconversion and the mechanism of switching remain to be established but are likely to be critical for comparing results from different experimental setups.

**3.2. Distance Measurements across the RNR  $\alpha/\beta$  Interface Using 94 GHz  $^{19}\text{F}$  ENDOR.** **3.2.1.  $^{19}\text{F}$  ENDOR Detects  $Y_{356}\bullet-^{19}\text{F}_{Y_{731}}$  Distances.**  $^{19}\text{F}$  ENDOR spectra of  $Y_{356}\bullet$  in  $F_3Y_{122}\beta_2/F_2Y_{731}\alpha_2$  (black) and  $E_{52}Q/F_3Y_{122}\beta_2/F_2Y_{731}\alpha_2$  (red) were obtained after summing three background-corrected, orientation-selective spectra in the range of  $\pm 4 \text{ MHz}$  around the  $^{19}\text{F}$  Larmor frequency  $\nu_0(^{19}\text{F})$  (Figure 5A). When using short  $\tau$  values (236 and 266 ns), prominent resonances are observed at  $\pm 0.8 \text{ MHz}$  in both samples. These resonances are attributed to one  $^{19}\text{F}$  nucleus,  $F_a$ , with a peak separation of  $\sim 1.6 \pm 0.1 \text{ MHz}$  (purple, dashed lines). Additionally, sharp features are observed in a  $\pm 250 \text{ kHz}$  region around  $\nu_0(^{19}\text{F})$ . These resonances were investigated using a larger  $\tau$  value of 620 ns, which enhances the sensitivity for

smaller couplings (Figure 5B).<sup>49</sup> For both samples, the spectra in Figure 5B can be interpreted as a superposition of two Pake patterns contributed by two  $^{19}\text{F}$  nuclei, designated as  $F_b$  and  $F_c$ . Pake patterns result from purely dipolar coupling and allow assignment of the corresponding dipolar HFC  $T$  by reading off the splitting between the sharp, central peaks:  $T_b = 250 \pm 15 \text{ kHz}$  (cyan, dashed lines) and  $T_c = 150 \pm 15 \text{ kHz}$  (green, dashed lines). These peaks are contributed by molecules in which the  $^{19}\text{F}$ -radical interspin vector is perpendicular to the external magnetic field  $B_0$ . Using the point-dipole approximation (eq 1)<sup>49</sup>

$$T = T_{\perp} = \frac{74.52}{R^3} \text{MHz} \cdot \text{\AA}^3 \quad (1)$$

we can estimate interspin distances of  $R_b = 6.7 \pm 0.2 \text{ \AA}$  and  $R_c = 7.9 \pm 0.3 \text{ \AA}$ , with the centroid of the O, C1, C3, and C5 atoms of  $Y_{356}\bullet$  as a point of reference.<sup>68</sup> Aside from the central peaks, Pake patterns are also characterized by shoulders appearing at twice the coupling strength ( $2 \cdot T = T_{\parallel}$ ). These features are contributed by molecules with interspin vectors parallel to  $B_0$ . The dipolar approximation does not apply for the stronger coupling  $T_a$  due to the shorter distance,  $< 5 \text{ \AA}$ .<sup>49</sup>

The observation of three distinct  $^{19}\text{F}$  resonances in Figure 5A,B requires at least two conformations of  $F_2Y_{731}$ . Since each conformation contributes two  $^{19}\text{F}-Y_{356}\bullet$  spin pairs, a fourth set of resonances ( $F_d$ ) is expected but not clearly resolved in the spectra obtained by summing up three orientation-selective measurements. An indication for coupling to a fourth nucleus  $F_d$  was provided by the orientation-selective measurements with  $B_0$  aligned along  $g_x$  (Figure 5C). Here, strong selectivity for the parallel components of  $F_b$  and  $F_c$  was observed. In addition, shoulders on the inside of the two most prominent features are observed, which suggest the parallel coupling of the fourth atom  $F_d$ . Further analysis of the orientation-selective spectra is discussed below and will confirm this assignment.

Interestingly, the size of the observed HFCs (peak positions) is conserved in both  $F_3Y_{122}\beta_2/F_2Y_{731}\alpha_2$  and  $E_{52}Q/F_3Y_{122}\beta_2/F_2Y_{731}\alpha_2$  mutants, but the spectrum of  $E_{52}Q/F_3Y_{122}\beta_2/F_2Y_{731}\alpha_2$  in Figure 5A appears broader, suggesting more heterogeneity in this mutant.

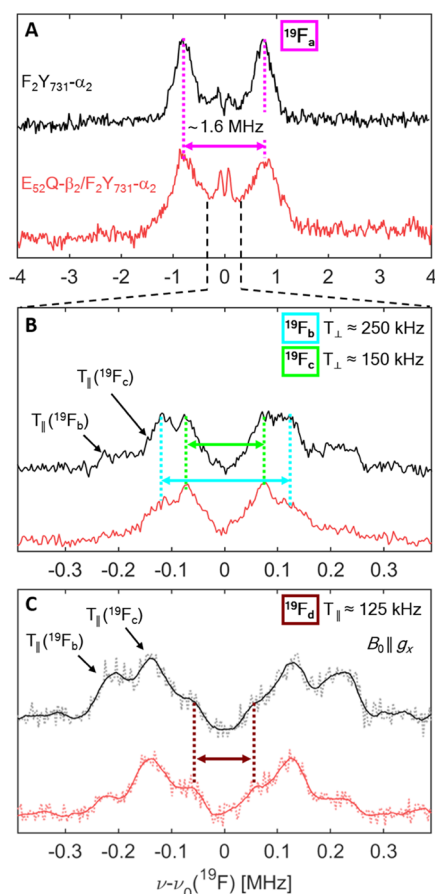


**Figure 5.** 94 GHz  $^{19}\text{F}$  Mims ENDOR spectra of  $\text{F}_3\text{Y}_{122}\text{-}\beta_2/\text{F}_2\text{Y}_{731}\text{-}\alpha_2$  ( $80\ \mu\text{M}$ ,  $T_Q = 50\ \text{s}$ , black lines) and  $\text{E}_{52}\text{Q}/\text{F}_3\text{Y}_{122}\text{-}\beta_2/\text{F}_2\text{Y}_{731}\text{-}\alpha_2$  ( $80\ \mu\text{M}$ ,  $T_Q = 35\ \text{s}$ , red lines) at  $T = 50\ \text{K}$ . Spectra in panels (A) and (B) were obtained by adding three orientation-selective spectra. (A) Measurement with short  $\tau$  values ( $\sim 250\ \text{ns}$ ). (B) Measurement with larger  $\tau$  values ( $\sim 620\ \text{ns}$ ). (C) Orientation-selective spectra with  $B_0$   $\parallel g_x$  and  $\tau = 620\ \text{ns}$  after data point smoothing with the Savitzky–Golay filter (full lines). Original data are shown as dotted lines. Measurement time per spectrum is 30–40 h (A) and 50–60 h (B). Analysis of the spectra in panels (A)–(C) requires consideration of four nuclei  $^{19}\text{F}_a$ – $^{19}\text{F}_d$ , as marked by arrows and colored dashed lines.

**3.2.2. Examination of Structural Models of the Triad  $\text{Y}_{730}\text{-F}_2\text{Y}_{731}\text{-Y}_{356}$ .** To rationalize the  $^{19}\text{F}$  ENDOR spectra, structural models of the tyrosine triad were built (Section 2.7 and Figure 3) and the DFT-predicted  $^{19}\text{F}$  HFCs were compared with the experimental values in Figure 5. The starting point for modeling is the cryo-EM structure.<sup>38</sup> Model S1 (Figure 3, black) is identical to this structure, with two  $^{19}\text{F}$  nuclei replacing the 3,5-H atoms in  $\text{Y}_{731}$ . This structure results in HFCs of 65 kHz and 114 kHz (see also SI 8, Table S8), the latter approaching but not quite matching the 150 kHz indicated for  $\text{F}_c$  in Figure 5B given DFT uncertainties up to 20%. The 65 kHz coupling could potentially be attributed to the fourth  $^{19}\text{F}$  nucleus,  $\text{F}_d$ .

To increase the coupling strength in S1, either the position of  $\text{F}_2\text{Y}_{731}$  or of  $\text{Y}_{356}$  had to be readjusted for the spin centers to come closer. An increase of  $T_c$  from 114 to  $\sim 150$  kHz for  $\text{F}_c$  would require reducing the interspin distance by roughly 1 Å based on eq 1. To maintain the stacked arrangement of  $\text{F}_2\text{Y}_{731}$  and  $\text{Y}_{730}$ , observed in almost all available structures, we adjusted the position of  $\text{O-Y}_{356}$  by ca. 1 Å, which is still well within the resolution of the cryo-EM structure, as indicated in

green color in Figure 3 (Table S6). This resulted in model S2, illustrated in Figure 6. We note that in model S2, as well as in

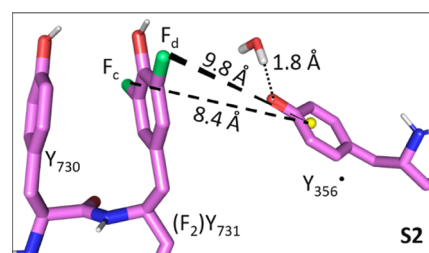


**Figure 6.** Model S2,  $^{19}\text{F}\text{-Y}_{356}$  distances are indicated by dashed lines (centroid of  $\text{Y}_{356}$  as a point of reference). Fluorine, oxygen, and nitrogen atoms are in green, red, and blue, respectively.  $\text{H}_2\text{O}$  was included based on our previous results.<sup>27,28</sup>

all other models, a water molecule was introduced in the vicinity of  $\text{Y}_{356}$  (Section 2.7), the presence of which was reported earlier.<sup>27,28</sup> The H-bonding water molecule affects  $\text{Y}_{356}$ 's spin density distribution and, consequently, also the effective  $^{19}\text{F}$ -radical HFCs. As detailed in SI 7, the resulting geometrical changes are minor and amount to ca. 0.1–0.2 Å.

In S2, the  $^{19}\text{F}\text{-Y}_{356}$  distances are 9.8 and 8.4 Å, the latter consistent with the estimate for  $\text{R}_c$  based on the dipolar approximation (eq 1). DFT analysis of S2 predicts coupling constants of 85 and 153 kHz, reproducing the coupling of  $\text{F}_c$  in Figure 5B within the estimated uncertainty. The 85 kHz coupling could be attributed to  $\text{F}_d$ . When the triad shown in S2 is incorporated back into the cryo-EM structure, the position of  $\text{Y}_{356}$  was found to fulfill the PELDOR diagonal distance of 3.0 nm (Figure 4 and Table S7).

Nevertheless, it is clear that neither model S2 nor reorienting the ring plane of  $\text{F}_2\text{Y}_{731}$  (model S3, Figure S16) is able to reproduce the observed strong HFCs of  $\text{F}_a$ .

We therefore examined the possibility that a second conformation between the interfacial Ys might result in a second pair of stronger  $^{19}\text{F}$  HFCs. This proposal is reasonable based on previous evidence from different types of experiments that  $\text{Y}_{731}$  can flip.<sup>23,26,30,44,45</sup> A small model based on the flipped Y-dyad taken from the X-ray structure of  $\text{NH}_2\text{Y}_{730}\text{-}\alpha_2$ <sup>44</sup> (without  $\beta_2$ ) could not be placed into the cryo-EM structure using pair fitting (in PyMOL) of the ring atoms to superimpose the  $\text{Y}_{730}$  side chains since clashes resulted (SI 8, Figure S17). This is in principle expected because this structure is missing the  $\beta$  subunit, which provides structural constraints. We thus focused on  $\alpha\beta$  and returned to model S2, adjusted the dihedral angles around  $\text{C}\alpha\text{-C}\beta$  and  $\text{N-C}\alpha$  of  $\text{Y}_{731}$  (Table S6), until the DFT-predicted HFC couplings reached the range of the experimental values for  $\text{F}_a$  and  $\text{F}_b$ . Representative structures that fulfilled the  $^{19}\text{F}$  HFCs are shown as models S4 and S5 (Figure 7), in which the fluorophenol groups are flipped by about 50–70° toward the subunit interface.

In S4 (Figure 7A,C), the  $^{19}\text{F}$  nuclei reside at distances of 4.1 and 6.8 Å from the centroid of  $\text{Y}_{356}$ . For the proximal  $^{19}\text{F}$  atom ( $\text{F}_a$ ), DFT predicts a dipolar coupling constant  $T_a$  of  $\sim 1.0$  MHz and a negative, isotropic coupling constant  $a_{\text{iso},a}$  of  $-0.8$  MHz. This combination leads to a splitting of  $\sim 1.8$  MHz for S4, similar to the  $\sim 1.6$  MHz observed experimentally for  $\text{F}_a$  (Figure 5A). The larger of the two  $^{19}\text{F}$ -radical distances in S4 agrees well with the estimate for  $\text{R}_b$ , yielding a coupling

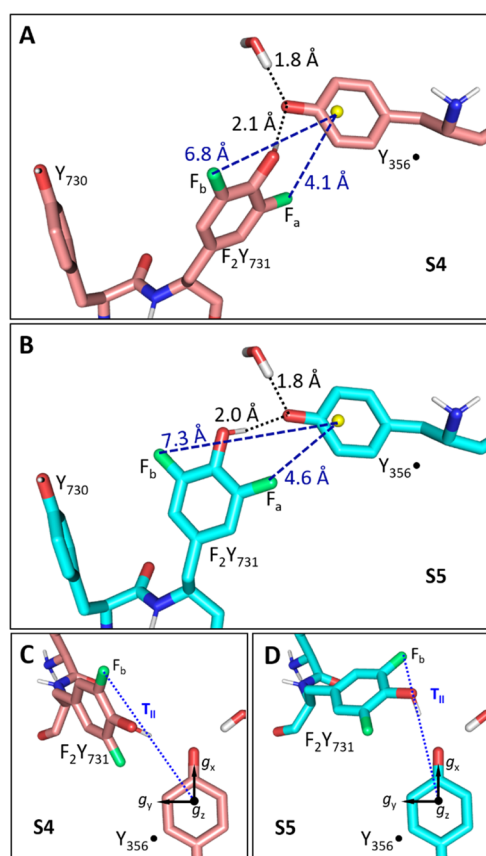


**Figure 7.** Models S4 (A) and S5 (B). (A) Model S4 (fluorine, oxygen, and nitrogen atoms in green, red, and blue, respectively). H-bond lengths and the  $^{19}\text{F}$ -centroid ( $\text{Y}_{356}$ , yellow sphere) distances are indicated. (B) Model S5 (cyan sticks, colors as in panel A). (C and D) Top view of the models shown in panels (A) and (B). In panels (C) and (D), the  $g$  tensor of  $\text{Y}_{356}$  is indicated along with the parallel component of the dipolar HFC tensor of the distal  $^{19}\text{F}$  nucleus  $\text{F}_b$ .

constant  $T_b$  of 254 kHz, in agreement with the resonances of  $\text{F}_b$  (Figure 5B).

In a second model with a flipped  $\text{Y}_{731}$  (S5, Figure 7B,D), a distinct orientation of  $\text{Y}_{731}$  and  $\text{Y}_{356}$  was considered to account for orientation selection (see also next section). In S5, the  $^{19}\text{F}$ – $\text{Y}_{356}$  distances are 4.6 and 7.3 Å. The interspin vector from the distal  $\text{F}_b$  to the centroid of  $\text{Y}_{356}$  is nearly parallel to the direction of  $g_x$  (Figure 7D) and distinct from S4 (Figure 7C). It has a DFT-derived HFC of  $T_b = 246$  kHz. For the proximal  $^{19}\text{F}$  nucleus  $\text{F}_a$ , a dipolar coupling constant of  $T_a \approx 0.8$  MHz with a negative isotropic coupling constants  $a_{\text{iso},a}$  of ca  $-1.0$  MHz is predicted and leads to an expected peak separation of  $\sim 1.8$  MHz as in S4.

A comparison of DFT-predicted HFCs from all models, S1–S5, and the experimental values is shown in Figure 8. More details on geometrical parameters of the five models are summarized in Table S7. We note that the combination of S2 with either S4 or S5 could satisfy the experimentally observed peak separations in Figure 5.

Finally, both S4 and S5, when integrated back into the framework of the cryo-EM structure,<sup>38</sup> give centroid–centroid distances between  $\text{F}_2\text{Y}_{731}$  in  $\alpha\beta$  and  $\text{F}_3\text{Y}_{122}$  in  $\alpha'\beta'$  of 35.0 and 35.5 Å, respectively, both very similar to the constraints measured in our previous PELDOR experiments.<sup>26</sup>

**3.2.3. Spectral Simulations Including a Superposition of Stacked and Flipped  $\text{Y}_{731}$  Conformations.** The DFT analysis

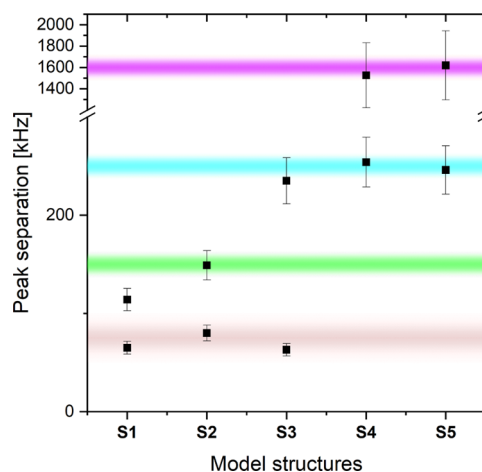


**Figure 8.** Comparison of experimentally observed peak separation from Figures 5 and 9 (purple ( $\text{F}_a$ ), cyan ( $\text{F}_b$ ), green ( $\text{F}_c$ ), and brown ( $\text{F}_d$ ) shadings indicate the range of uncertainty) with DFT-predicted peak positions (black squares) for models S1–S5. For the DFT values, an error of  $\pm 20\%$  ( $\text{F}_a$ , this nucleus exhibits isotropic and anisotropic coupling) or  $\pm 10\%$  ( $\text{F}_b$ – $\text{F}_d$ , these nuclei show purely dipolar coupling) is estimated.

indicated that it is possible to find mutual conformations of  $\text{F}_2\text{Y}_{731}$  and  $\text{Y}_{356}$ , which individually satisfy some observed  $^{19}\text{F}$ – $\text{Y}_{356}$  distances. To examine whether a superposition of these conformations can reproduce the ENDOR spectra, we also considered the orientation-selected ENDOR spectra, which pose additional constraints with respect to the sum spectra of Figure 5.

Representative orientation-selected spectra, corresponding to the black sum spectra of Figure 5, are displayed in Figure 9. In the small coupling region (Figure 9B), we observe that  $T_{\parallel}(\text{F}_b)$  appears enhanced at  $g_x$ , suggesting an orientation of the  $\text{F}_b$  dipolar tensor parallel to  $g_x$ . Therefore, a structure similar to S5 likely describes the data better than S4, as illustrated in Figure 7C,D, where the orientation of the dipolar vector with respect to  $g_x$  is displayed.

Using these orientational constraints, global simulations of the orientation-selective ENDOR spectra based on models S2 and S5 were carried out with the DFT-predicted parameters listed in Table 1 and the ratio (i.e., the relative contribution of S2 and S5) varied until a minimum of residual could be found (SI 9). rmsd from these simulations for all samples amount to ca. 0.1 or 10% at the optimized ratios (Figure S18). We observed that the simulation of the large coupling  $\text{F}_a$  (Figure 9A) is not very sensitive to the weighting of S2 and S5. This is expected as, under those experimental conditions, the resonances of  $\text{F}_b$ – $\text{F}_d$  are suppressed by the Mims blind spot in the center of the spectrum. Instead, the ratio  $\text{F}_b/\text{F}_c$  affects the simulations of the small coupling region, as can be seen in Figure 9B by the decomposition of the simulation into the individual contributions. We note that the obtained weighting of the flipped conformation slightly varies between samples from 18 to 33% within an error of 5% for each sample (Table 2). Therefore, we estimate that the flipped conformation represents on average  $25 \pm 10\%$  of the molecular ensemble.

The representative best simulation for one sample  $\text{F}_3\text{Y}_{122}$ – $\beta_2/\text{F}_2\text{Y}_{731}$ – $\alpha_2$  is superimposed on the experimental data in Figure 9. Remarkably, the simulation of the orientation-selective spectrum at  $B_0 \parallel g_x$  captures the selectivity for  $T_{\parallel}(\text{F}_b)$  and  $T_{\parallel}(\text{F}_c)$  and also reproduces the shoulders on the inner

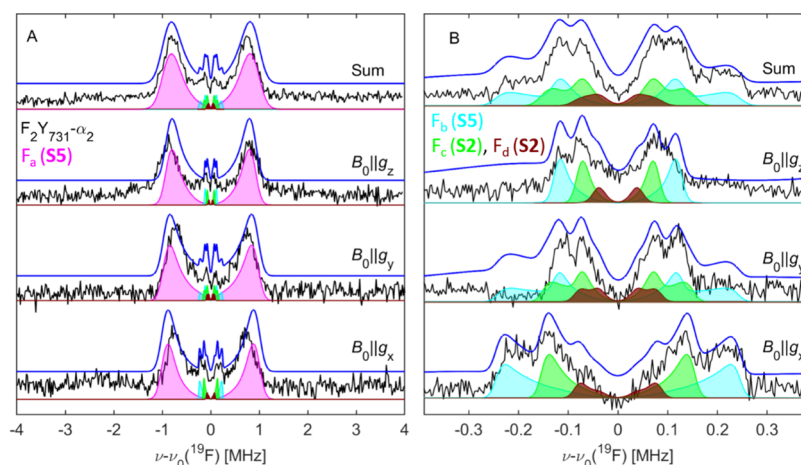


**Figure 9.** 94 GHz  $^{19}\text{F}$  Mims ENDOR spectra on  $\text{F}_3\text{Y}_{122}\text{-}\beta_2/\text{F}_2\text{Y}_{731}\text{-}\alpha_2$  ( $80\ \mu\text{M}$ ,  $T_Q = 50\ \text{s}$ , black lines) at  $T = 50\ \text{K}$ . (A) Measurement with short  $\tau$  values ( $\sim 250\ \text{ns}$ ). (B) Measurement with larger  $\tau$  values ( $\sim 620\ \text{ns}$ ). Simulations including four different  $^{19}\text{F}$  atoms ( $\text{F}_a\text{-}\text{F}_d$ ) are shown as blue lines and are based on S2 and S5 (Tables 1 and 2). Contributions of individual  $^{19}\text{F}$  atoms are shown as shaded areas: purple ( $\text{F}_a$ ), cyan, ( $\text{F}_b$ ), green ( $\text{F}_c$ ), and brown ( $\text{F}_d$ ).

**Table 1. Parameters Used for the ENDOR Simulations**

atom (model)	$\text{F-Y}_{356}^{\bullet a}$ [Å]	$A_x, A_y, A_z^b$ [kHz]	$a_{\text{iso}}$ [kHz]
$\text{F}_a$ (S5)	4.6	580, -1668, -1952	-1013
$\text{F}_b$ (S5)	7.3	-246, -246, 492	0
$\text{F}_c$ (S2)	8.4	-159, -159, 318	0
$\text{F}_d$ (S2)	10.0	-83, -83, 166	0

<sup>a</sup>Distances defined with respect to the centroid of  $\text{Y}_{356}^{\bullet}$ , as shown in Figures 6 and 7B. <sup>b</sup>Coupling constants  $A_i$  consider the anisotropic and the isotropic coupling constants ( $T_i$  and  $a_{\text{iso}}$ , respectively):  $A_i = T_i + a_{\text{iso}}$ . Euler angles for relating the  $A$  to  $g$  tensors are reported in Table S8. An error of  $\pm 15\ \text{kHz}$  was estimated for couplings  $< 500\ \text{kHz}$ , while an error of  $\pm 125\ \text{kHz}$  is estimated for the 1.6 MHz coupling (ca. 50% of the ENDOR line width parameter in both cases).

**Table 2. Ratios of the Stacked Model S2 and the Flipped Model S5 from ENDOR Simulations**

RNR mutant	$T_Q$ [s]	contribution of flipped (S5) <sup>a</sup>
$\text{F}_3\text{Y}_{122}\text{-}\beta_2/\text{F}_2\text{Y}_{731}\text{-}\alpha_2$	50	33%
$\text{F}_3\text{Y}_{122}\text{-}\beta_2/\text{F}_2\text{Y}_{731}\text{-}\alpha_2$	143	22%
$\text{E}_{52}\text{Q}/\text{F}_3\text{Y}_{122}\text{-}\beta_2/\text{F}_2\text{Y}_{731}\text{-}\alpha_2$	35	18%
$\text{E}_{52}\text{Q}/\text{F}_3\text{Y}_{122}\text{-}\beta_2/\text{F}_2\text{Y}_{731}\text{-}\alpha_2$	153	25%

<sup>a</sup>Estimated error:  $\pm 5\%$ ; see Figure S18.

side, which were tentatively assigned to  $\text{F}_d$  in the discussion of Figure 5C. Given the challenges of the simulation procedure, we find that the obtained simulation reproduces the experimental data very satisfactorily.

**3.3.  $^{17}\text{O}$  ENDOR with ( $\text{E}_{52}\text{Q}$ )- $\text{F}_3\text{Y}_{122}\text{-}\beta_2/^{17}\text{O}\text{-Y}\text{-wt}\text{-}\alpha_2$ .** An independent effort was made to obtain experimental evidence for a flipped  $\text{Y}_{731}$  conformation in the trapped complex. We investigated whether a  $^{17}\text{O}$  ENDOR signal might be observable with a sample prepared using uniformly labeled  $^{17}\text{O}\text{-Y}\text{-wt}\text{-}\alpha_2$  ( $^{17}\text{O}$  in the phenol groups). This experiment was motivated by our recent successful observation of a  $^{17}\text{O}$  ENDOR signal from water H-bonded to  $\text{Y}_{356}^{\bullet}$ .<sup>28</sup> DFT calculations predicted a  $^{17}\text{O}\text{-Y}_{731}\text{-Y}_{356}^{\bullet}$  coupling of  $\sim 0.5\ \text{MHz}$  for the flipped structure S5, slightly smaller than observed for H-bonded  $^{17}\text{OH}_2$  (0.7 MHz) (Table S9). We further considered issues that might make detection of this interaction more challenging.  $^{17}\text{O}$  has a lower gyromagnetic ratio than  $^{19}\text{F}$  ( $\gamma(^{19}\text{F})/\gamma(^{17}\text{O}) \approx 6.95$ ) and its

quadrupolar coupling may lead to signal broadening. In addition, the  $^{17}\text{O}\text{-Y}_{731}\text{-}\alpha_2$  is only 35–40%-labeled based on the available  $^{17}\text{O}\text{-Y}$  used during expression (SI 6). A reference ENDOR signal, with a comparable concentration of predicted  $^{17}\text{O}$  spins in close proximity to  $\text{Y}_{356}^{\bullet}$  (i.e., ca 10–20  $\mu\text{M}$ ), is shown in Figure S15. Despite potential unexpected issues, we proceeded with the experiment as  $^{17}\text{O}$  should be a sensitive nucleus at short distances ( $\lesssim 3\ \text{Å}$ ) and the  $^{17}\text{O}\text{-Y}_{731}$  coupling for the stacked conformation should not be detectable, allowing us to test the flipped  $\text{Y}_{731}$  model. As shown in SI 6.2, we were not able to observe any  $^{17}\text{O}$  couplings in three independently prepared samples. We have considered several possible explanations for these observations that may be related either to the experiment or to the use of  $\text{F}_n\text{Y}$  probes: (1) the  $^{17}\text{O}$  coupling might be smaller than the DFT prediction and not detectable; (2)  $\text{F}_2\text{Y}_{731}$  could experience a different flipping ratio or rate of flipping relative to  $\text{Y}_{731}$ ; (3) the  $\text{F}_3\text{Y}_{122}^{\bullet}$  used to initiate radical transfer in the experiment is likely reduced to its phenolate, not phenol as with  $\text{Y}_{122}^{\bullet}$ , and could play a role for the subunit interaction. These scenarios will be further discussed in the next section.

## 4. DISCUSSION

In this paper, we report the use of 94 GHz  $^{19}\text{F}$  ENDOR spectroscopy, which has provided new insight into the chemistry of RT between  $\text{Y}_{356}(\beta)$  and  $\text{Y}_{731}(\alpha)$  of *E. coli* RNR located at the subunit interface (Figure 2C,D). Success was possible using enzymes with site-specifically incorporated  $\text{F}_n\text{Y}$ s:  $\text{F}_3\text{Y}_{122}\text{-}\beta_2$  (or  $\text{E}_{52}\text{Q}/\text{F}_3\text{Y}_{122}\text{-}\beta_2$ ) and  $\text{F}_2\text{Y}_{731}\text{-}\alpha_2$ , which, when incubated with substrate (GDP) and effector (TTP), allowed trapping of the  $\text{Y}_{356}^{\bullet}$  pathway radical in an “active”  $\alpha_2\beta_2$  complex during the reverse RT pathway process. PELDOR and HF-EPR analysis established the location of the trapped radical, and the double mutant provided a direct link to the recent cryo-EM structure.<sup>38</sup> The studies allowed measurement of the  $^{19}\text{F}\text{-Y}_{731}$  hyperfine couplings to  $\text{Y}_{356}^{\bullet}$ , which report on their interspin distances and provide interesting mechanistic implications.

Analysis of 94 GHz  $^{19}\text{F}$  ENDOR spectra of the  $\text{Y}_{356}^{\bullet}$  required careful evaluation and subtraction of  $^{19}\text{F}$  signals associated with unreduced  $\text{F}_3\text{Y}_{122}^{\bullet}$  and  $^1\text{H}$  backgrounds.



Nevertheless, comparison of the spectra acquired at 50 and 80 K allowed unambiguous assignment of three distinct couplings between  $F_2Y_{731}$  and  $Y_{356}^\bullet$ .

Construction of small models of the three Ys and their DFT-predicted  $^{19}\text{F}$  HFC couplings, ENDOR orientation selection, and spectral simulations indicated that the  $^{19}\text{F}$  spectra are consistent with a mixture of flipped and stacked conformations of  $F_2Y_{731}$  with respect to  $Y_{730}$ , with flipped contributions of  $25 \pm 10\%$  among the samples. While the flexibility of  $Y_{731}$  has been reported previously, the present results provide the first evidence for a conformation, in which the two pathway residues are located at an O–O distance of  $\sim 3$  Å, with potentially important consequences for understanding the interfacial PCET step. The presence of both conformations simultaneously suggests that they are energetically similar and may exist in equilibrium.

A number of different types of experiments have previously reported multiple  $Y_{731}$  conformations.<sup>26,30</sup> In one study, in which CDP/ATP was incubated with *wt*- $\beta_2$ /R<sub>411</sub>A-NH<sub>2</sub>Y<sub>731</sub>- $\alpha_2$ , an NH<sub>2</sub>Y<sub>731</sub> $^\bullet$  intermediate trapped in the forward RT was observed.<sup>26</sup> The flipping was detected by PELDOR spectroscopy by its unusual  $Y_{356}^\bullet$ /NH<sub>2</sub>Y<sub>731</sub> $^\bullet$  distance. This distance, however, was only observed in conjunction with an additional mutation at  $\alpha$ -R<sub>411</sub>A. This residue sits in the  $\alpha/\beta$  interface. In addition, transient absorption experiments in solution using the same  $\alpha$ -R<sub>411</sub>A mutation and a photo-oxidant indicated a  $k_{\text{PCET}}$  between  $Y_{356}\text{F-photo}\beta_2$  and  $Y_{731}$  much faster than dNDP formation,  $\sim 10^4$  s<sup>-1</sup> versus  $1-10$  s<sup>-1</sup>.<sup>30</sup>

On the other hand, neither in the cryo-EM structure with E<sub>52</sub>Q/F<sub>3</sub>Y<sub>122</sub>- $\beta_2$  nor in the  $^{17}\text{O}$  ENDOR experiments, which both employed F<sub>3</sub>Y<sub>122</sub> $^\bullet$  and *wt*- $\alpha_2$ , was the flipped conformation of  $Y_{731}$  observed. Thus, while the role of  $F_2Y_{731}$  in potentiating flipping is still unclear, the F<sub>3</sub>-phenolate generated at residue 122 during RT may not be the basis for a flipped  $Y_{731}$  conformation. In addition, the conditions for freeze-quenching the cryo-EM and ENDOR samples are very distinct in terms of protein concentration and glycerol content. A protein concentration of  $\sim 80$   $\mu\text{M}$  had to be used for EPR samples, exceeding physiological RNR concentrations (ca. 1  $\mu\text{M}$ ). At elevated protein concentrations, the formation of  $\alpha_4\beta_4$  complexes has been reported.<sup>69,70</sup> However, these complexes are incapable of producing  $Y_{356}^\bullet$  and should not affect the analysis of EPR experiments, in which  $Y_{356}^\bullet$  was observed selectively.

Overall, the complex interplay between  $Y_{356}(\beta)$ ,  $Y_{731}(\alpha)$ , R<sub>411</sub>( $\alpha$ ), and other residues at the subunit interface is likely to be crucial for regulating the communication between the two redox-active Ys across the  $\alpha/\beta$  interface.

Inspecting the predicted HFC parameters of the phenolic proton of  $F_2Y_{731}$  with respect to  $Y_{356}^\bullet$  is another interesting source of information. The DFT calculations predicted HFCs of  $\sim 6$  MHz in models S4 and S5. It is important to rationalize this finding in the context of previous  $^1\text{H}$  ENDOR studies on H-bond interactions to  $Y_{356}^\bullet$ .<sup>27</sup> In those studies, a  $^1\text{H}$  coupling in the range of 6 MHz was observed and assigned to one (or 2 equiv) H-bonded water molecule(s). The presence of the second water molecule was postulated to explain the unprecedented low  $g_x$  value of  $Y_{356}^\bullet$ , i.e., 2.0062.<sup>27</sup> The sharp peaks observed in our recent 263 GHz  $^{17}\text{O}$  ENDOR experiments support the presence of only a single water molecule.<sup>28</sup> Given the similarity of coupling constants for the H-bonded protons for  $Y_{731}$  from either model S4 or S5, the flipped conformation provides an explanation for the  $^1\text{H}$

coupling consistent with these previous  $^1\text{H}$  ENDOR data. To date, however, no ENDOR study has provided information on the interplay between stacked/flipped  $Y_{731}$  and the water binding at  $Y_{356}^\bullet$ , which may be a key feature to control PCET across the interface. Interestingly, no distribution of  $g_x$  values at  $Y_{356}^\bullet$  is observed, indicating that the electrostatic environment is well defined and similar in both  $Y_{731}$  conformations. A mechanism, by which  $Y_{731}$  replaces a water molecule as a H-bond donor to  $Y_{356}^\bullet$  upon flipping, could explain this finding.

#### 4.1. Implication of Flipped $Y_{731}$ in PCET across $\alpha/\beta$ .

Observation of flipped  $F_2Y_{731}$  in close distance to  $Y_{356}^\bullet$ , trapped in an active RNR complex, enables the examination of a mechanism for the PCET step between  $Y_{356}^\bullet$  and  $Y_{731}$  for the first time.

The current hypothesis for interfacial PCET involving water, as noted above, was based on the ENDOR studies and the H-bond to  $Y_{356}^\bullet$  assigned to water.<sup>27,28</sup> Recent MD simulations<sup>45</sup> based on the cryo-EM structure supported the role of water first suggested by Nick et al.<sup>27</sup> The simulations additionally showed that water molecules can be present at the  $\alpha/\beta$  interface including between  $Y_{356}$  and  $Y_{731}$ , between  $Y_{356}$  and  $\beta$ -E<sub>52</sub> (an interface residue), and support a pathway for water to escape to the bulk solvent.<sup>38,45</sup> Interestingly, MD also revealed an equilibrium between flipped and stacked conformation for  $Y_{731}$ , both populated at room temperature.<sup>45</sup> Nevertheless, the reported flipped  $Y_{731}$  structure from the MD study still shows a long O–O distance to  $Y_{356}$  ( $\sim 8$  Å on average), precluding a direct interaction between the two Ys.<sup>45</sup>

Thus, the mechanism of PCET between  $Y_{356}$  and  $Y_{731}$  (i.e., during reverse and forward RTs) remained to be resolved due to the long  $Y_{356}$ – $Y_{731}$  distance ( $\sim 8$  Å) observed in the cryo-EM structure.<sup>38</sup> We note that the published cryo-EM structure and ENDOR data have distinct problems. The resolution of the cryo-EM structure was insufficient to resolve waters. The ENDOR studies only detected water in the first coordination sphere of  $Y_{356}^\bullet$ , i.e., in a distance range of  $\sim 3$  Å.<sup>27,28</sup>

The  $^{19}\text{F}$  ENDOR data presented here, despite the issues raised, provide evidence for close interaction between the two Ys across the subunit interface in an active RNR construct. In our ENDOR-derived model S5, the O–O distance between  $Y_{356}^\bullet$ – $Y_{731}$  amounts to  $3.0 \pm 0.2$  Å, with a similar value in the related model S4. This distance is within the range of the distances reported for the pathway pair C<sub>439</sub>– $Y_{730}$  (O–S: 3.7 Å in the X-ray structure of  $\alpha_2$  versus 3.4 Å in  $\alpha$ -NH<sub>2</sub>Y<sub>730</sub>)<sup>13,44</sup> as well as for the pair  $Y_{730}$ – $Y_{731}$  (O–O: 3.3 Å in  $\alpha_2$  versus 2.7 Å in  $\alpha$ -NH<sub>2</sub>Y<sub>730</sub>).<sup>13,44</sup> For these pairs, independent quantum chemical calculations predicted a colinear PCET mechanism,<sup>24,71,72</sup> in which the electron and proton are transferred individually in one step from the same donor to the same acceptor, although a water-assisted PCET has been proposed and discussed for the C<sub>439</sub>– $Y_{730}$  pair.<sup>73</sup> Recently, also an alternative, glutamate (E<sub>623</sub>)-mediated proton transfer for the RT between  $Y_{731}$  and  $Y_{730}$ , has been proposed based on MD simulations and QM/MM analysis.<sup>74</sup> A key conclusion from the latter study based on the analysis of E<sub>623</sub> was that forward and reverse RTs are different. Interestingly, our earlier large-scale DFT calculation on the pathway triad C<sub>439</sub>– $Y_{730}$ – $Y_{731}$  predicted that the coordination of a water molecule to  $Y_{730}^\bullet$  can stabilize this radical intermediate and the transition states to the next pathway intermediates,  $Y_{731}^\bullet$  and C<sub>439</sub> $^\bullet$ .<sup>24</sup> Therefore, the calculation pointed to a functional role of water in PCET without its direct involvement as a proton donor or acceptor. Based on these considerations, we propose

that our current results are consistent with a model of colinear PCET mechanism for the RT  $Y_{356}^{\bullet}(\beta) - Y_{731}(\alpha) \rightleftharpoons Y_{356}(\beta) - Y_{731}^{\bullet}(\alpha)$ . This mechanism requires a conformational change of  $Y_{731}$  during the long-range RT, as the next step ( $Y_{731}^{\bullet}(\alpha) - Y_{730}(\alpha) \rightleftharpoons Y_{731}(\alpha) - Y_{730}^{\bullet}(\alpha)$ ) occurs in the stacked conformation of the  $Y_{731}/Y_{730}$  pair.

## 5. CONCLUSIONS

Use of site-specifically incorporated unnatural amino acids and kinetic trapping in conjunction with high-field ENDOR, PELDOR, and EPR spectroscopies has given new insight into the PCET involving  $Y_{356}^{\bullet}(\beta)$  and  $Y_{731}(\alpha)$  across the RNR subunit interface.  $^{19}\text{F}$  ENDOR revealed two sets of hyperfine coupling constants for  $\text{F}_2\text{Y}_{731}$  caused by the occurrence of two distinct conformations. One set of hyperfine couplings is consistent with a stacked  $Y_{731}$  conformation at an  $\sim 8$  Å distance (O–O) to  $Y_{356}^{\bullet}$ , as observed by cryo-EM. However, much larger  $^{19}\text{F}$  couplings revealed a second conformation, in which  $\text{F}_2\text{Y}_{731}$  is flipped toward  $Y_{356}^{\bullet}$  at a much shorter O–O distance of  $\sim 3$  Å. This distance is similar to distances between other Y pairs on the RT pathway in  $\alpha$ , for which colinear PCET has been established.

These results reveal again the ability and importance of EPR spectroscopic methods and new experimental designs for the detection of multiple conformations in a biological machinery.

## ■ ASSOCIATED CONTENT

### SI Supporting Information

The Supporting Information is available free of charge at <https://pubs.acs.org/doi/10.1021/jacs.2c02906>.

Measurement of RNR activity, EPR sample preparation, EPR experiments (263, 34, and 94 GHz spectroscopies including relaxation measurements, radical yield determination, and background corrections),  $^{17}\text{O}$  ENDOR data, modeling of the tyrosine triad, and ENDOR simulations (PDF)

## ■ AUTHOR INFORMATION

### Corresponding Authors

**Andreas Meyer** – Research group ESR spectroscopy, Max Planck Institute for Multidisciplinary Sciences, 37077 Göttingen, Germany; Email: [Andreas.meyer@mpinat.mpg.de](mailto:Andreas.meyer@mpinat.mpg.de)

**JoAnne Stubbe** – Department of Chemistry and Department of Biology, Massachusetts Institute of Technology, Cambridge, Massachusetts 20139, United States; [orcid.org/0000-0001-8076-4489](https://orcid.org/0000-0001-8076-4489); Email: [stubbe@mit.edu](mailto:stubbe@mit.edu)

**Marina Bennati** – Research group ESR spectroscopy, Max Planck Institute for Multidisciplinary Sciences, 37077 Göttingen, Germany; Department of Chemistry, Georg-August University, 37077 Göttingen, Germany; [orcid.org/0000-0001-6784-7845](https://orcid.org/0000-0001-6784-7845); Email: [Marina.Bennati@mpinat.mpg.de](mailto:Marina.Bennati@mpinat.mpg.de)

### Authors

**Annamarie Kehl** – Research group ESR spectroscopy, Max Planck Institute for Multidisciplinary Sciences, 37077 Göttingen, Germany; [orcid.org/0000-0002-6105-8252](https://orcid.org/0000-0002-6105-8252)

**Chang Cui** – Department of Chemistry and Chemical Biology, Harvard University, Cambridge, Massachusetts 02138, United States; [orcid.org/0000-0002-4709-7458](https://orcid.org/0000-0002-4709-7458)

**Fehmke A. K. Reichardt** – Research group ESR spectroscopy, Max Planck Institute for Multidisciplinary Sciences, 37077 Göttingen, Germany

**Fabian Hecker** – Research group ESR spectroscopy, Max Planck Institute for Multidisciplinary Sciences, 37077 Göttingen, Germany; [orcid.org/0000-0001-7262-5497](https://orcid.org/0000-0001-7262-5497)

**Lisa-Marie Funk** – Department of structural dynamics, Max Planck Institute for Multidisciplinary Sciences, 37077 Göttingen, Germany; Department of Molecular Enzymology, Georg-August University, 37077 Göttingen, Germany

**Manas K. Ghosh** – Department of Chemistry and Chemical Biology, Harvard University, Cambridge, Massachusetts 02138, United States; Present Address: Department of Chemistry, Texas A&M University, College Station, Texas 77843, United States.

**Kuan-Ting Pan** – Research group bioanalytical mass spectrometry, Max Planck Institute for Multidisciplinary Sciences, 37077 Göttingen, Germany; Bioanalytics, University Medical Center, 37075 Göttingen, Germany; Present Address: Department of Medicine II, Hematology/Oncology, University Hospital Frankfurt, 60590 Frankfurt, Germany; Present Address: Frankfurt Cancer Institute, Goethe University Frankfurt, 60596 Frankfurt, Germany; [orcid.org/0000-0001-6974-5324](https://orcid.org/0000-0001-6974-5324)

**Henning Urlaub** – Research group bioanalytical mass spectrometry, Max Planck Institute for Multidisciplinary Sciences, 37077 Göttingen, Germany; Bioanalytics, University Medical Center, 37075 Göttingen, Germany

**Kai Tittmann** – Department of structural dynamics, Max Planck Institute for Multidisciplinary Sciences, 37077 Göttingen, Germany; Department of Molecular Enzymology, Georg-August University, 37077 Göttingen, Germany; [orcid.org/0000-0001-7891-7108](https://orcid.org/0000-0001-7891-7108)

Complete contact information is available at: <https://pubs.acs.org/doi/10.1021/jacs.2c02906>

## Funding

The authors acknowledge funding from the Max Planck Society, the German DFG priority program SPP 1601, the ERC-BIO-enMR grant (contract 101020262), a fellowship of the graduate school GGNB (A.K., program Physics of Biological and Complex Systems), and the NIH grants GM047274 (C.C.) and GM-29595 (J.S. and C.C.). Open access funded by Max Planck Society.

## Notes

The authors declare no competing financial interest. Original spectroscopic data associated with Figures <sup>5</sup> and <sup>9</sup> as well as all xyz coordinates of the model structures can be accessed via the open database Göttingen Research Online (<https://doi.org/10.25625/YXHC63>).

## ■ ACKNOWLEDGMENTS

The authors thank Dr. M. Hiller for the initial recording of 263 GHz and Anna Doppler for assistance in EPR sample preparation and initial PELDOR measurements. J.S. would like to thank Dan Nocera for the continuous discussions about PCET and his comments on this manuscript. Sabine König is acknowledged for assistance with the mass spectrometry experiments. Dr. Dalvin Méndez-Hernández and Prof. Dr. Ana L. Moore are gratefully acknowledged for providing their structural models of water-binding phenoxyl radicals.

## REFERENCES

- (1) Hofer, A.; Crona, M.; Logan, D. T.; Sjöberg, B.-M. DNA Building Blocks: Keeping Control of Manufacture. *Crit. Rev. Biochem. Mol. Biol.* **2012**, *47*, 50–63.
- (2) Nordlund, P.; Reichard, P. Ribonucleotide Reductases. *Annu. Rev. Biochem.* **2006**, *75*, 681–706.
- (3) Stubbe, J.; Nocera, D. G. Radicals in Biology: Your Life Is in Their Hands. *J. Am. Chem. Soc.* **2021**, *143*, 13463–13472.
- (4) Aye, Y.; Li, M.; Long, M.; Weiss, R. Ribonucleotide Reductase and Cancer: Biological Mechanisms and Targeted Therapies. *Oncogene* **2015**, *34*, 2011–2021.
- (5) Zimanyi, C. M.; Chen, P. Y.-T.; Kang, G.; Funk, M. A.; Drennan, C. L. Molecular Basis for Allosteric Specificity Regulation in Class Ia Ribonucleotide Reductase from *Escherichia Coli*. *eLife* **2016**, *5*, No. e07141.
- (6) Greene, B. L.; Kang, G.; Cui, C.; Bennati, M.; Nocera, D. G.; Drennan, C. L.; Stubbe, J. Ribonucleotide Reductases: Structure, Chemistry, and Metabolism Suggest New Therapeutic Targets. *Annu. Rev. Biochem.* **2020**, *89*, 45–75.
- (7) Baker, C. H.; Banzon, J.; Bollinger, J.; Stubbe, J.; Samano, V.; Robins, M.; Lippert, B.; Jarvi, E.; Resvick, R. 2'-Deoxy-2'-Methylenecytidine and 2'-Deoxy-2', 2'-Difluorocytidine 5'-Diphosphates: Potent Mechanism-Based Inhibitors of Ribonucleotide Reductase. *J. Med. Chem.* **1991**, *34*, 1879–1884.
- (8) Hertel, L. W.; Boder, G. B.; Kroin, J. S.; Rinzel, S. M.; Poore, G. A.; Todd, G. C.; Grindey, G. B. Evaluation of the Antitumor Activity of Gemcitabine (2', 2'-Difluoro-2'-Deoxycytidine). *Cancer Res.* **1990**, *50*, 4417–4422.
- (9) Narasimhan, J.; Letinski, S.; Jung, S. P.; Gerasyuto, A.; Wang, J.; Arnold, M.; Chen, G.; Hedrick, J.; Dumble, M.; Ravichandran, K.; Levitz, T.; Cui, C.; Drennan, C. L.; Stubbe, J.; Karp, G.; Branstrom, A. Ribonucleotide Reductase, a Novel Drug Target for Gonorrhea. *eLife* **2022**, *11*, No. e67447.
- (10) Dutia, B. M.; Frame, M. C.; Subak-Sharpe, J. H.; Clark, W. N.; Marsden, H. S. Specific Inhibition of Herpesvirus Ribonucleotide Reductase by Synthetic Peptides. *Nature* **1986**, *321*, 439–441.
- (11) Shao, J.; Zhou, B.; Chu, B.; Yen, Y. Ribonucleotide Reductase Inhibitors and Future Drug Design. *Curr. Cancer Drug Targets* **2006**, *6*, 409–431.
- (12) Aye, Y.; Stubbe, J. Clofarabine 5'-Di and-Triphosphates Inhibit Human Ribonucleotide Reductase by Altering the Quaternary Structure of Its Large Subunit. *Proc. Natl. Acad. Sci. U.S.A.* **2011**, *108*, 9815–9820.
- (13) Uhlin, U.; Eklund, H. Structure of Ribonucleotide Reductase Protein R1. *Nature* **1994**, *370*, 533–539.
- (14) Nordlund, P.; Eklund, H. Structure and Function of the *Escherichia Coli* Ribonucleotide Reductase Protein R2. *J. Mol. Biol.* **1993**, *232*, 123–164.
- (15) Minnihan, E. C.; Nocera, D. G.; Stubbe, J. Reversible, Long-Range Radical Transfer in *E. Coli* Class Ia Ribonucleotide Reductase. *Acc. Chem. Res.* **2013**, *46*, 2524–2535.
- (16) Hammes-Schiffer, S. Proton-Coupled Electron Transfer: Moving Together and Charging Forward. *J. Am. Chem. Soc.* **2015**, *137*, 8860–8871.
- (17) Cukier, R. I.; Nocera, D. G. Proton-Coupled Electron Transfer. *Annu. Rev. Phys. Chem.* **1998**, *49*, 337–369.
- (18) Reece, S. Y.; Nocera, D. G. Proton-Coupled Electron Transfer in Biology: Results from Synergistic Studies in Natural and Model Systems. *Annu. Rev. Biochem.* **2009**, *78*, 673–699.
- (19) Stubbe, J.; Nocera, D. G.; Yee, C. S.; Chang, M. C. Radical Initiation in the Class I Ribonucleotide Reductase: Long-Range Proton-Coupled Electron Transfer? *Chem. Rev.* **2003**, *103*, 2167–2202.
- (20) Bennati, M.; Weber, A.; Antonic, J.; Perlstein, D. L.; Robblee, J.; Stubbe, J. Pulsed ELDOR Spectroscopy Measures the Distance between the Two Tyrosyl Radicals in the R2 Subunit of the *E. Coli* Ribonucleotide Reductase. *J. Am. Chem. Soc.* **2003**, *125*, 14988–14989.
- (21) Bennati, M.; Robblee, J. H.; Mugnaini, V.; Stubbe, J.; Freed, J. H.; Borbat, P. EPR Distance Measurements Support a Model for Long-Range Radical Initiation in *E. Coli* Ribonucleotide Reductase. *J. Am. Chem. Soc.* **2005**, *127*, 15014–15015.
- (22) Seyedsayamdost, M. R.; Chan, C. T.; Mugnaini, V.; Stubbe, J.; Bennati, M. PELDOR Spectroscopy with DOPA- $\beta$ 2 and NH<sub>2</sub>Y- $\alpha$ 2s: Distance Measurements between Residues Involved in the Radical Propagation Pathway of *E. Coli* Ribonucleotide Reductase. *J. Am. Chem. Soc.* **2007**, *129*, 15748–15749.
- (23) Yokoyama, K.; Smith, A. A.; Corzilius, B.; Griffin, R. G.; Stubbe, J. Equilibration of Tyrosyl Radicals (Y<sub>356</sub><sup>•</sup>, Y<sub>731</sub><sup>•</sup>, Y<sub>730</sub><sup>•</sup>) in the Radical Propagation Pathway of the *Escherichia Coli* Class Ia Ribonucleotide Reductase. *J. Am. Chem. Soc.* **2011**, *133*, 18420–18432.
- (24) Argirevic, T.; Riplinger, C.; Stubbe, J.; Neese, F.; Bennati, M.; ENDOR; Spectroscopy; Calculations, DFT. Evidence for the Hydrogen-Bond Network within  $\alpha$ 2 in the PCET of *E. Coli* Ribonucleotide Reductase. *J. Am. Chem. Soc.* **2012**, *134*, 17661–17670.
- (25) Nick, T. U.; Lee, W.; Koßmann, S.; Neese, F.; Stubbe, J.; Bennati, M. Hydrogen Bond Network between Amino Acid Radical Intermediates on the Proton-Coupled Electron Transfer Pathway of *E. Coli*  $\alpha$ 2 Ribonucleotide Reductase. *J. Am. Chem. Soc.* **2015**, *137*, 289–298.
- (26) Kasanmascheff, M.; Lee, W.; Nick, T. U.; Stubbe, J.; Bennati, M. Radical Transfer in *E. Coli* Ribonucleotide Reductase: A NH<sub>2</sub>Y<sub>731</sub>/R<sub>411</sub>A- $\alpha$  Mutant Unmasks a New Conformation of the Pathway Residue 731. *Chem. Sci.* **2016**, *7*, 2170–2178.
- (27) Nick, T. U.; Ravichandran, K. R.; Stubbe, J.; Kasanmascheff, M.; Bennati, M. Spectroscopic Evidence for a H Bond Network at Y<sub>356</sub> Located at the Subunit Interface of Active *E. Coli* Ribonucleotide Reductase. *Biochemistry* **2017**, *56*, 3647–3656.
- (28) Hecker, F.; Stubbe, J.; Bennati, M. Detection of Water Molecules on the Radical Transfer Pathway of Ribonucleotide Reductase by <sup>17</sup>O Electron–Nuclear Double Resonance Spectroscopy. *J. Am. Chem. Soc.* **2021**, *143*, 7237–7241.
- (29) Pokern, Y.; Eltzner, B.; Huckemann, S. F.; Beeken, C.; Stubbe, J.; Tkach, I.; Bennati, M.; Hiller, M. Statistical Analysis of ENDOR Spectra. *Proc. Natl. Acad. Sci. U.S.A.* **2021**, *118*, No. e2023615118.
- (30) Greene, B. L.; Taguchi, A. T.; Stubbe, J.; Nocera, D. G. Conformationally Dynamic Radical Transfer within Ribonucleotide Reductase. *J. Am. Chem. Soc.* **2017**, *139*, 16657–16665.
- (31) Holder, P. G.; Pizano, A. A.; Anderson, B. L.; Stubbe, J.; Nocera, D. G. Deciphering Radical Transport in the Large Subunit of Class I Ribonucleotide Reductase. *J. Am. Chem. Soc.* **2012**, *134*, 1172–1180.
- (32) Song, D. Y.; Pizano, A. A.; Holder, P. G.; Stubbe, J.; Nocera, D. G. Direct Interfacial Y<sub>731</sub> Oxidation in  $\alpha$ 2 by a Photo $\beta$ 2 Subunit of *E. Coli* Class Ia Ribonucleotide Reductase. *Chem. Sci.* **2015**, *6*, 4519–4524.
- (33) Cui, C.; Greene, B. L.; Kang, G.; Drennan, C. L.; Stubbe, J.; Nocera, D. G. Gated Proton Release during Radical Transfer at the Subunit Interface of Ribonucleotide Reductase. *J. Am. Chem. Soc.* **2021**, *143*, 176–183.
- (34) Greene, B. L.; Stubbe, J.; Nocera, D. G. Photochemical Rescue of a Conformationally Inactivated Ribonucleotide Reductase. *J. Am. Chem. Soc.* **2018**, *140*, 15744–15752.
- (35) Climent, I.; Sjöberg, B. M.; Huang, C. Y. Carboxyl-Terminal Peptides as Probes for *Escherichia Coli* Ribonucleotide Reductase Subunit Interaction: Kinetic Analysis of Inhibition Studies. *Biochemistry* **1991**, *30*, 5164–5171.
- (36) Climent, I.; Sjöberg, B. M.; Huang, C. Y. Site-Directed Mutagenesis and Deletion of the Carboxyl Terminus of *Escherichia Coli* Ribonucleotide Reductase Protein R2. Effects on Catalytic Activity and Subunit Interaction. *Biochemistry* **1992**, *31*, 4801–4807.
- (37) Sjöberg, B. M.; Karlsson, M.; Jörnvall, H. Half-Site Reactivity of the Tyrosyl Radical of Ribonucleotide Reductase from *Escherichia Coli*. *J. Biol. Chem.* **1987**, *262*, 9736–9743.

- (38) Kang, G.; Taguchi, A. T.; Stubbe, J.; Drennan, C. L. Structure of a Trapped Radical Transfer Pathway within a Ribonucleotide Reductase Holoenzyme. *Science* **2020**, *368*, 424–427.
- (39) Lin, Q.; Parker, M. J.; Taguchi, A. T.; Ravichandran, K.; Kim, A.; Kang, G.; Shao, J.; Drennan, C. L.; Stubbe, J. Glutamate 52- $\beta$  at the  $\alpha/\beta$  Subunit Interface of *Escherichia Coli* Class Ia Ribonucleotide Reductase is Essential for Conformational Gating of Radical Transfer. *J. Biol. Chem.* **2017**, *292*, 9229–9239.
- (40) Roy, B.; Decout, J.-L.; Béguin, C.; Fontecave, M.; Allard, P.; Kuprin, S.; Ehrenberg, A. NMR Studies of Binding of 5-FdUDP and DCDP to Ribonucleoside-Diphosphate Reductase from *Escherichia Coli*. *Biochim. Biophys. Acta, Protein Struct. Mol. Enzymol.* **1995**, *1247*, 284–292.
- (41) Ravichandran, K.; Minnihan, E. C.; Lin, Q.; Yokoyama, K.; Taguchi, A. T.; Shao, J.; Nocera, D. G.; Stubbe, J. Glutamate 350 Plays an Essential Role in Conformational Gating of Long-Range Radical Transport in *Escherichia Coli* Class Ia Ribonucleotide Reductase. *Biochemistry* **2017**, *56*, 856–868.
- (42) Ravichandran, K. R.; Taguchi, A. T.; Wei, Y.; Tommos, C.; Nocera, D. G.; Stubbe, J. A >200 meV Uphill Thermodynamic Landscape for Radical Transport in *Escherichia Coli* Ribonucleotide Reductase Determined Using Fluorotyrosine-Substituted Enzymes. *J. Am. Chem. Soc.* **2016**, *138*, 13706–13716.
- (43) Glover, S. D.; Parada, G. A.; Markle, T. F.; Ott, S.; Hammarström, L. Isolating the Effects of the Proton Tunneling Distance on Proton-Coupled Electron Transfer in a Series of Homologous Tyrosine-Base Model Compounds. *J. Am. Chem. Soc.* **2017**, *139*, 2090–2101.
- (44) Minnihan, E. C.; Seyedsayamdost, M. R.; Uhlin, U.; Stubbe, J. Kinetics of Radical Intermediate Formation and Deoxyribonucleotide Production in 3-Aminotyrosine-Substituted *Escherichia Coli* Ribonucleotide Reductases. *J. Am. Chem. Soc.* **2011**, *133*, 9430–9440.
- (45) Reinhardt, C. R.; Li, P.; Kang, G.; Stubbe, J.; Drennan, C. L.; Hammes-Schiffer, S. Conformational Motions and Water Networks at the  $\alpha/\beta$  Interface in *E. Coli* Ribonucleotide Reductase. *J. Am. Chem. Soc.* **2020**, *142*, 13768–13778.
- (46) Ravichandran, K. R.; Zong, A. B.; Taguchi, A. T.; Nocera, D. G.; Stubbe, J.; Tommos, C. Formal Reduction Potentials of Difluorotyrosine and Trifluorotyrosine Protein Residues: Defining the Thermodynamics of Multistep Radical Transfer. *J. Am. Chem. Soc.* **2017**, *139*, 2994–3004.
- (47) Reinhardt, C. R.; Sequeira, R.; Tommos, C.; Hammes-Schiffer, S. Computing Proton-Coupled Redox Potentials of Fluorotyrosines in a Protein Environment. *J. Phys. Chem. B* **2021**, *125*, 128–136.
- (48) Wells, G. B.; Makinen, M. W. ENDOR-Determined Molecular Geometries of Spin-Labeled Fluoroanilides in Frozen Solution. *J. Am. Chem. Soc.* **1988**, *110*, 6343–6352.
- (49) Meyer, A.; Dechert, S.; Dey, S.; Höbartner, C.; Bennati, M. Measurement of Angstrom to Nanometer Molecular Distances with  $^{19}\text{F}$  Nuclear Spins by EPR/ENDOR Spectroscopy. *Angew. Chem., Int. Ed.* **2020**, *59*, 373–379.
- (50) Minnihan, E. C.; Young, D. D.; Schultz, P. G.; Stubbe, J. Incorporation of Fluorotyrosines into Ribonucleotide Reductase Using an Evolved, Polyspecific Aminoacyl-tRNA Synthetase. *J. Am. Chem. Soc.* **2011**, *133*, 15942–15945.
- (51) Thelander, L.; Sjöberg, B.-M.; Eriksson, S. Ribonucleoside Diphosphate Reductase (*Escherichia Coli*). In *Methods in Enzymology*; Academic Press, 1978; Vol. 51, pp 227–237.
- (52) Tkach, I.; Bejenke, I.; Hecker, F.; Kehl, A.; Kusanmascheff, M.; Gromov, I.; Prisecaru, I.; Höfer, P.; Hiller, M.; Bennati, M.  $^1\text{H}$  High Field Electron-Nuclear Double Resonance Spectroscopy at 263 GHz/9.4 T. *J. Magn. Reson.* **2019**, *303*, 17–27.
- (53) Martin, R. E.; Pannier, M.; Diederich, F.; Gramlich, V.; Hubrich, M.; Spiess, H. W. Determination of End-to-end Distances in a Series of TEMPO Diradicals of up to 2.8 Nm Length with a New Four-pulse Double Electron Electron Resonance Experiment. *Angew. Chem., Int. Ed.* **1998**, *37*, 2833–2837.
- (54) Pannier, M.; Veit, S.; Godt, A.; Jeschke, G.; Spiess, H. W. Dead-Time Free Measurement of Dipole–Dipole Interactions between Electron Spins. *J. Magn. Reson.* **2011**, *213*, 316–325.
- (55) Jeschke, G.; Chechik, V.; Ionita, P.; Godt, A.; Zimmermann, H.; Banham, J.; Timmel, C.; Hilger, D.; Jung, H. DeerAnalysis2006—a Comprehensive Software Package for Analyzing Pulsed ELDOR Data. *Appl. Magn. Reson.* **2006**, *30*, 473–498.
- (56) Chiang, Y.-W.; Borbat, P. P.; Freed, J. H. The Determination of Pair Distance Distributions by Pulsed ESR Using Tikhonov Regularization. *J. Magn. Reson.* **2005**, *172*, 279–295.
- (57) Worswick, S. G.; Spencer, J. A.; Jeschke, G.; Kuprov, I. Deep Neural Network Processing of DEER Data. *Sci. Adv.* **2018**, *4*, No. eaat5218.
- (58) Epel, B.; Arieli, D.; Baute, D.; Goldfarb, D. Improving W-Band Pulsed ENDOR Sensitivity—Random Acquisition and Pulsed Special TRIPLE. *J. Magn. Reson.* **2003**, *164*, 78–83.
- (59) Bruggemann, W.; Niklas, J. R. Stochastic ENDOR. *J. Magn. Reson., Ser. A* **1994**, *108*, 25–29.
- (60) Rizzato, R.; Kaminker, I.; Vega, S.; Bennati, M. Cross-Polarisation Edited ENDOR. *Mol. Phys.* **2013**, *111*, 2809–2823.
- (61) Stoll, S.; Schweiger, A. EasySpin, a Comprehensive Software Package for Spectral Simulation and Analysis in EPR. *J. Magn. Reson.* **2006**, *178*, 42–55.
- (62) Kehl, A.; Hiller, M.; Hecker, F.; Tkach, I.; Dechert, S.; Bennati, M.; Meyer, A. Resolution of Chemical Shift Anisotropy in  $^{19}\text{F}$  ENDOR Spectroscopy at 263 GHz/9.4 Tesla. *J. Magn. Reson.* **2021**, No. 107091.
- (63) DeLano, W. L. Pymol: An Open-Source Molecular Graphics Tool. *CCP4 Newsl. Protein Crystallogr.* **2002**, *40*, 82–92.
- (64) Neese, F. The ORCA Program System. *Wiley Interdiscip. Rev.: Comput. Mol. Sci.* **2012**, *2*, 73–78.
- (65) Lucarini, M.; Mugnaini, V.; Pedulli, G. F.; Guerra, M. Hydrogen-Bonding Effects on the Properties of Phenoxy Radicals. An EPR, Kinetic, and Computational Study. *J. Am. Chem. Soc.* **2003**, *125*, 8318–8329.
- (66) Méndez-Hernández, D. D.; Baldansuren, A.; Kalendra, V.; Charles, P.; Mark, B.; Marshall, W.; Molnar, B.; Moore, T. A.; Lakshmi, K.; Moore, A. L. HYSCORE and DFT Studies of Proton-Coupled Electron Transfer in a Bioinspired Artificial Photosynthetic Reaction Center. *iScience* **2020**, *23*, No. 101366.
- (67) Ravichandran, K. R.; Minnihan, E. C.; Wei, Y.; Nocera, D. G.; Stubbe, J. Reverse Electron Transfer Completes the Catalytic Cycle in a 2,3,5-Trifluorotyrosine-Substituted Ribonucleotide Reductase. *J. Am. Chem. Soc.* **2015**, *137*, 14387–14395.
- (68) Riplinger, C.; Kao, J. P.; Rosen, G. M.; Kathirvelu, V.; Eaton, G. R.; Eaton, S. S.; Kutateladze, A.; Neese, F. Interaction of Radical Pairs Through-Bond and through-Space: Scope and Limitations of the Point–Dipole Approximation in Electron Paramagnetic Resonance Spectroscopy. *J. Am. Chem. Soc.* **2009**, *131*, 10092–10106.
- (69) Ando, N.; Brignole, E. J.; Zimanyi, C. M.; Funk, M. A.; Yokoyama, K.; Asturias, F. J.; Stubbe, J.; Drennan, C. L. Structural Interconversions Modulate Activity of *Escherichia Coli* Ribonucleotide Reductase. *Proc. Natl. Acad. Sci. U.S.A.* **2011**, *108*, 21046–21051.
- (70) Zimanyi, C. M.; Ando, N.; Brignole, E. J.; Asturias, F. J.; Stubbe, J.; Drennan, C. L. Tangled up in Knots: Structures of Inactivated Forms of *E. Coli* Class Ia Ribonucleotide Reductase. *Structure* **2012**, *20*, 1374–1383.
- (71) Siegbahn, P. E. M.; Eriksson, L.; Himo, F.; Pavlov, M. Hydrogen Atom Transfer in Ribonucleotide Reductase (RNR). *J. Phys. Chem. B* **1998**, *102*, 10622–10629.
- (72) Kaila, V. R. I.; Hummer, G. Energetics of Direct and Water-Mediated Proton-Coupled Electron Transfer. *J. Am. Chem. Soc.* **2011**, *133*, 19040–19043.
- (73) Chen, X.; Ma, G.; Sun, W.; Dai, H.; Xiao, D.; Zhang, Y.; Qin, X.; Liu, Y.; Bu, Y. Water Promoting Electron Hole Transport between Tyrosine and Cysteine in Proteins via a Special Mechanism: Double Proton Coupled Electron Transfer. *J. Am. Chem. Soc.* **2014**, *136*, 4515–4524.

(74) Reinhardt, C. R.; Sayfutyarova, E. R.; Zhong, J.; Hammes-Schiffer, S. Glutamate Mediates Proton-Coupled Electron Transfer Between Tyrosines 730 and 731 in *Escherichia Coli* Ribonucleotide Reductase. *J. Am. Chem. Soc.* **2021**, *143*, 6054–6059.

#### ■ NOTE ADDED AFTER ASAP PUBLICATION

This paper published ASAP on June 2, 2022 with a missing author (Manas K. Ghosh). The paper was corrected and the revised manuscript reposted on June 17, 2022.